

RESEARCH ARTICLE

10.1002/2013JE004558

Key Points:

- The spreading of water sills is limited by ice fracturing
- Deep sills can thicken significantly in contrast to shallow sills
- Pits, domes, and small chaos morphology can result from subsequent sill evolution

Correspondence to:

C. Michaut,
michaut@ipgg.fr

Citation:

Michaut, C., and M. Manga (2014), Domes, pits, and small chaos on Europa produced by water sills, *J. Geophys. Res. Planets*, 119, doi:10.1002/2013JE004558.

Received 14 OCT 2013

Accepted 12 FEB 2014

Accepted article online 14 FEB 2014

Domes, pits, and small chaos on Europa produced by water sills

Chloé Michaut¹ and Michael Manga²

¹Sciences Spatiales et Planétologie, Institut de Physique du Globe de Paris, Université Paris Diderot, Sorbonne Paris Cité, Paris, France, ²Department of Earth and Planetary Science, University of California, Berkeley, California, USA

Abstract Pits, domes, and small chaos on Europa's surface are quasi-circular features a few to a few tens of kilometers in diameter. We examine if injection of water sills into Europa's ice shell and their subsequent evolution can induce successive surface deformations similar to the morphologies of these features. We study the dynamics of water spreading within the elastic part of the ice shell and show that the mechanical properties of ice exert a strong control on the lateral extent of the sill. At shallow depths, water makes room for itself by lifting the overlying ice layer and water weight promotes lateral spreading of the sill. In contrast, a deep sill bends the underlying elastic layer and its weight does not affect its spreading. In that case, the sill lateral extent is limited by the fracture toughness of ice and the sill can thicken substantially. After emplacement, cooling of the sill warms the surrounding ice and thins the overlying elastic ice layer. As a result, preexisting stresses in the elastic part of the ice shell increase locally to the point that they may disrupt the ice above the sill (small chaos). Disruption of the surface also allows for partial isostatic compensation of water weight, leading to a topographic depression at the surface (pit), of the order of $\sim 10^2$ m. Complete water solidification finally causes expansion of the initial sill volume and results in an uplifted topography (dome) of $\sim 10^2$ m.

1. Introduction

The surface of Europa is littered with quasi-circular features a few to a few tens of kilometers in diameter. They may be uplifted (positive relief "domes") or depressed relative to their surroundings (negative relief "pits"). In some cases they show evidence of resurfacing or disruption of the crust (small "chaos"). As these features have an endogenic origin they provide an opportunity to study properties of, and processes within, Europa's ice shell.

Figure 1 shows a region containing many of these features. Given that pits, domes, and features with a disrupted surface occur in the same region and have similar sizes, "the principle of parsimony would guide us to seek a simple explanation for all of these features together, rather than separate explanations for each type of feature" [Collins and Nimmo, 2009, p. 260]. That is, can pits, domes, and small chaos all be the surface expression of a fundamentally similar internal process with their morphologies reflecting different stages of evolution?

The ice shell on Europa may be thick enough to undergo solid state convection in the warm ice that underlies a largely stagnant lithosphere [McKinnon, 1999; Barr and Showman, 2009]. The upwellings and downwellings produced by this convection have been invoked to explain the surface deformation at pits and domes [Rathbun et al., 1998; Pappalardo et al., 1998]. The magnitude of convectively produced temperature anomalies in the solid ice, however, is too small to produce the observed surface deformation [Nimmo and Manga, 2002; Showman and Han, 2004]. Hence, additional tidal heating [Han and Showman, 2010], melting [Head and Pappalardo, 1999; Sotin et al., 2002; Schmidt et al., 2011], or thermochemical convection [Pappalardo and Barr, 2004; Han and Showman, 2005] must be invoked. The general assessment is that near-surface weakening or compositional buoyancy are required to produce large relief [Barr and Showman, 2009].

If pits, domes, and small chaos do all share a common origin, the disruption of the crust to create isolated blocks of ice that can be rotated and tilted requires that liquid water was present at or near the surface [Spaun et al., 1998; Carr et al., 1998]. Melting the ice shell all the way from the subsurface ocean to the surface, sometimes referred to as melt-through [Greenberg et al., 1999; O'Brien et al., 2002], is energetically [Goodman et al., 2004] and rheologically [Nimmo et al., 2003] challenging. As a consequence, near-surface melting induced by convective motions inside the ice shell has been proposed. Melting could be induced

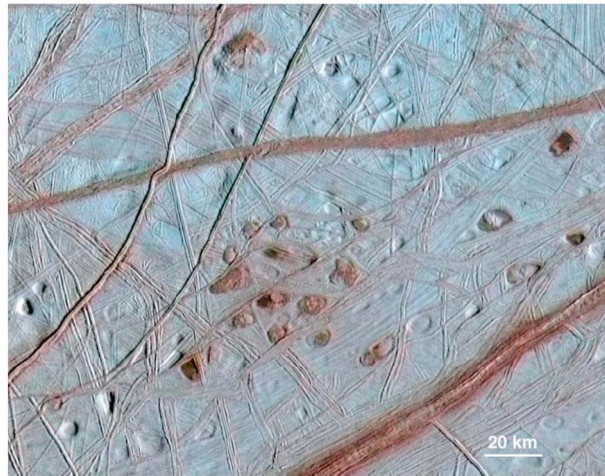


Figure 1. Image of domes and pits on Europa. Illumination from the right. NASA photojournal image PIA03878.

by enhanced tidal dissipation in rising plumes [Sotin *et al.*, 2002] or by eutectic melting of salty ice above a thermal plume [Schmidt *et al.*, 2011]. In the latter case, the decrease in specific volume of water as it melts would produce pits above subsurface lenses of water [Schmidt *et al.*, 2011]. It is not clear, however, why raised topography of domes, comparable in magnitude to the negative relief of pits [Singer *et al.*, 2010], should result from refreezing of this water as there is no net addition of mass to the ice shell. In addition the very low surface temperature of Europa limits melting above upwellings, making it difficult to generate thick lenses of water [Nimmo and Giese, 2005].

Another means of bringing liquid to the near-surface is by injecting horizontal bodies of water, called sills, within the ice shell. Formation of sills from a pressurized ocean was proposed by Collins *et al.* [2000], and ocean pressure produced by thickening the ice shell could become large enough to make sills [Manga and Wang, 2007]. Water sills have also been implicated in the formation of double ridges [Craft *et al.*, 2013; Dombard *et al.*, 2012]. “Compared to (other) mechanisms, sill injection has not been extensively studied” and “the horizontal extent of likely sills on Europa has not been modeled” [Collins and Nimmo, 2009, p 277]. The goal of the present study is to develop a model for the emplacement of sills within a shell of ice and to compute the expected surface topography and stresses at all stages during the emplacement and eventual solidification of water sills. With a quantitative model, we can then evaluate whether water sills, at different stages of evolution, may be responsible for pits, domes, and small chaos.

2. Conceptual Model Based on Timescales of Processes Involved in Sill Intrusion

Injection of water into an ice shell involves several mechanical and thermal processes including water intrusion, water cooling and solidification, compensation of water weight through flexural support, disruption of the ice shell, and topographic relaxation. There are several distinct timescales involved in each of these processes, and hence different mechanical and thermal processes dominate over these different timescales.

Figure 2 illustrates conceptually the different stages in the emplacement and solidification of the sill. The first stage is the intrusion of water into the part of the ice shell that deforms elastically, at least on emplacement timescales (stage 1). If the sill is intruded deep enough, it will deform the ice-ocean boundary and this topography will relax by viscous flow (stage 2). After emplacement, the water in the sill will start to freeze. The heat transferred to the surrounding ice will decrease the thickness of the elastic layer above the sill, increasing preexisting stresses in the ice shell resulting from the global cooling and solidification of the ocean [Nimmo, 2004; Manga and Wang, 2007] and possibly disrupting the ice shell (stage 3). The dense water sill will sag downward, supported by the strength of the underlying ice. Compensation of this internal load will depress the surface of Europa, forming a pit (stage 4). Final solidification of the sill and the volume expansion of the water will raise the surface, forming a dome (stage 5), provided that complete isostatic equilibrium was not achieved in stage 4. However, if the ice underneath the sill is heated to the point that it can no longer provide elastic support, water might sink as a diapir before complete solidification and return to the ocean.

Where does the water in the sill originate? One possible source is the ocean that underlies the ice shell. As the ice shell cools and thickens, thermal contraction and volume expansion of ice generate large stresses [Nimmo, 2004] and will increase ocean pressure [Manga and Wang, 2007] until the ice shell fails and forms a hydrofracture. At this point, water is injected into the ice shell as a vertical dike. Gas buoyancy from gas exsolution can also help water rise through dykes in the ice shell [Crawford and Stevenson, 1988]. Transitions

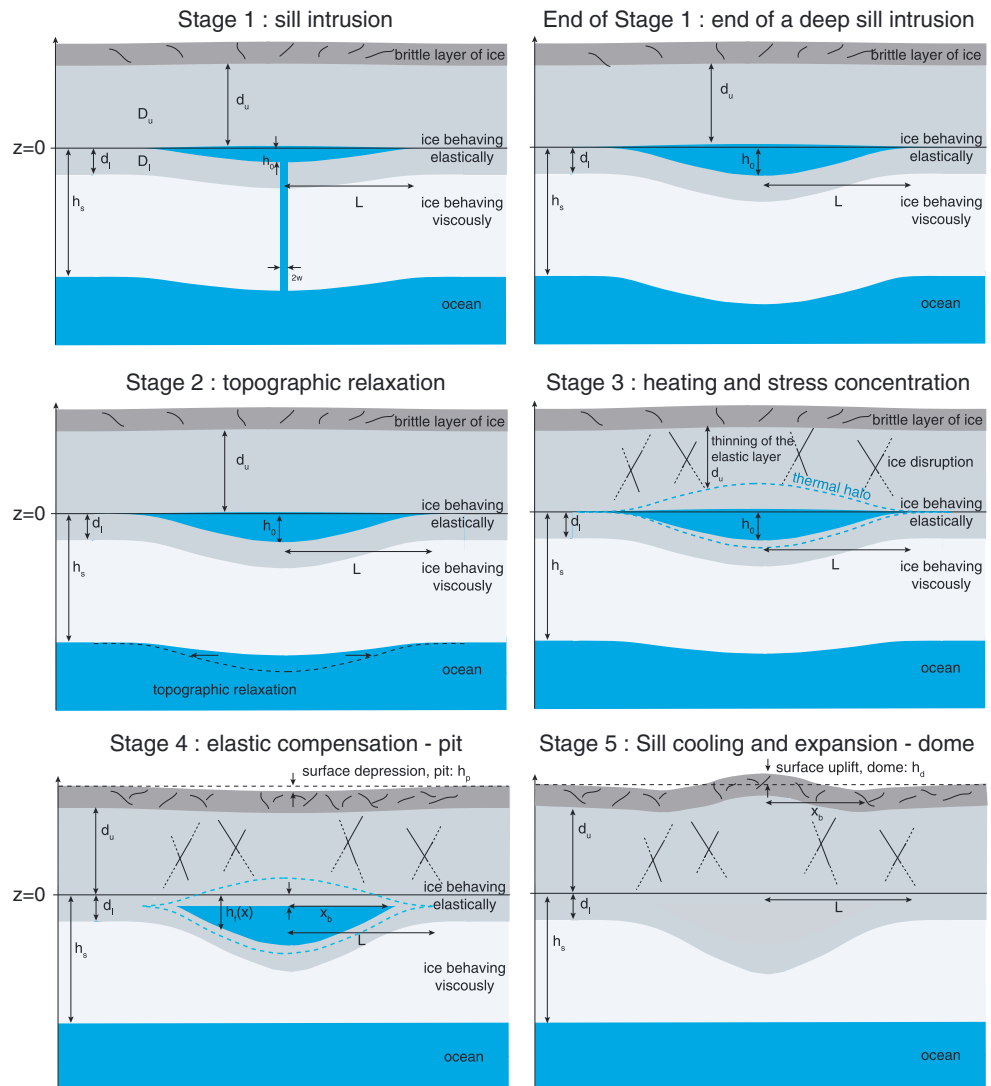


Figure 2. Succession of the different stages involved in sill emplacement and evolution in Europa's ice shell. As an alternative to elastic compensation (stage 4), the sill might sink back through the underlying viscous ice as a diapir, if the ice underneath the sill is heated to the point that it can no longer support the sill's weight elastically.

to horizontal intrusion occur when the dike encounters stresses unfavorable for propagation, e.g., compression in the upper part of the ice shell from thermal contraction [Nimmo, 2004], interfaces and discontinuities where the ice becomes stiffer [Gudmundsson, 2011, chap. 13.4], or a density barrier produced by an increase in porosity in near-surface ice. Neither the stress nor stiffness distribution are known well enough to identify the depth at which a dike would be deflected, and so we consider a range of possible depths. Other suggested sources of water for a sill include other solidifying bodies of water in the ice shell [Fagents, 2003] or melting of ice above a warm, rising diapir [Schmidt et al., 2011].

In the following sections, we examine each stage separately, model the evolution of the sill's lateral extent with time, and deduce the resulting surface topography. The thermal and mechanical processes that govern sill emplacement are coupled and complex, involving fracture propagation, turbulent flow, and elastic deformation in an ice shell in which thermal and rheological properties vary in space and time. In our analysis we thus focus on limits in which different mechanical and thermal processes dominate; our results and scalings are therefore best viewed as order of magnitude estimates but nevertheless provide a quantification of the different elements in the conceptual model (Figure 2).

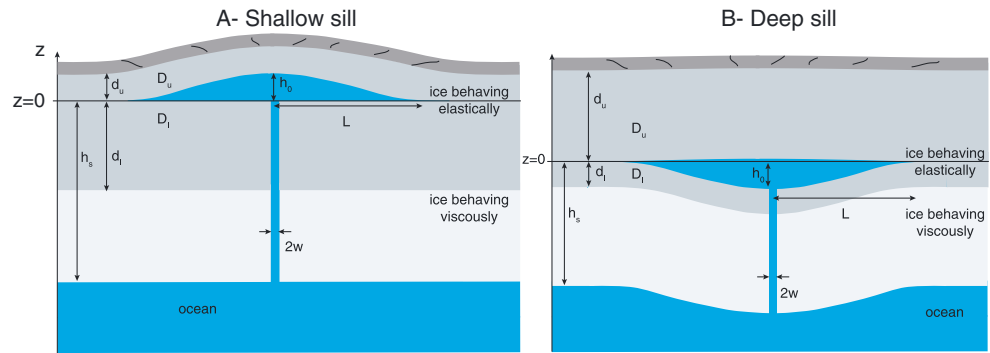


Figure 3. Geometry of sill emplacement at (a) shallow and (b) deep depths.

3. Dynamics of Sill Emplacement

The deformation of the ice shell in response to intrusion of a sill depends on the depth of intrusion and thickness of the ice shell. The total thickness of the ice shell is not known, is likely time variable [Husmann *et al.*, 2002], and is the subject of some debate. The thickness of the elastic part of the shell (on long timescales) is constrained by observations of flexurally supported features. A compilation of published values, however, indicates great variability from hundreds of meters to a few kilometers [Billings and Kattenhorn, 2005; Nimmo and Manga, 2009]. The equilibrium thickness of Europa's ice shell has a conductive layer extending to depths of ~ 10 km thick for a wide range of ice rheologies [Ruiz, 2010]. Given that pits, domes, and chaos are among the younger features on Europa [Pappalardo *et al.*, 1998], assuming an ice shell thickness similar to equilibrium values seems reasonable. For an ice shell in which heat transfer occurs by conduction in the upper 10 km, the base of the region that will deform elastically on sill emplacement timescales is 4 to 6 km below the surface (Appendix A).

We model sill intrusion within the ice shell considering two end-member cases. In the first case, the sill intrudes at shallow depth and the water makes room for itself by lifting the overlying ice, the "roof" (Figure 3a). In the second case, the sill intrudes at large depth within the ice shell; the roof of the intrusion has an elastic thickness, d_u , much larger than the one of its base, d_i , and the water makes room for itself by bending the lower elastic layer (Figure 3b). We evaluate the sill morphologies obtained in those two scenarios. We consider a two-dimensional geometry with a sill that is fed by a central dyke at a constant rate. The case of an axisymmetric sill is examined in Appendix B.

3.1. Water Intrusion Rate Into the Sill

The timescale to emplace the sill is

$$\tau_{\text{inject}} = V/Q_0, \quad (1)$$

where V is the volume of the sill and Q_0 is the injection rate.

The injection rate will depend on the overpressure in the ocean ΔP_0 driving water ascent and on the height of sill emplacement in the shell h_s . Bernoulli's equation for a perfect fluid gives at height z in the feeder dyke

$$\Delta P(z) + (\rho_w - \rho_i)gz + \frac{1}{2}\rho_w v_w^2(z) = C, \quad (2)$$

where C is a constant, ρ is density, g is gravity, v is velocity, and subscripts w and i indicate liquid water and ice, respectively. The maximum velocity that can be reached at the top of the dyke, i.e., at $z = 0$, using $v_w(z = -h_s) = 0$, is thus

$$v_w = \left(\frac{2(\Delta P_0 - (\rho_w - \rho_i)gh_s)}{\rho_w} \right)^{1/2}. \quad (3)$$

This estimate gives an upper bound for the velocity since friction on the wall is neglected. The driving overpressure ΔP_0 vanishes quickly as water ascends through the ice shell: to traverse a 10 km ice shell, ΔP_0 should be $> 10^6$ Pa.

Table 1. Model Parameters and Values

Parameter	Value	Reference
Fracture toughness K_c^a	0.1–0.3 MPa m ^{1/2}	<i>Litwin et al.</i> [2012]
Young's modulus E	1–5 × 10 ⁹ Pa	<i>Nimmo</i> [2004]
Shear modulus G	3.5 × 10 ⁹	<i>Moore and Schubert</i> [2000]
Poisson ratio ν	0.33	<i>Schulson</i> [2001]
Water compressibility β	5 × 10 ⁻¹⁰ Pa ⁻¹	<i>Fine and Millero</i> [1973]
Water density ρ_w	1000 kg m ⁻³	
Ice density ρ_i	910 kg m ⁻³	
Water viscosity μ_w	1.8 × 10 ⁻³ Pa s	
Ice activation energy Q^*	60 kJ mol ⁻¹	<i>Goldsby and Kohlstedt</i> [2001]
Ice reference viscosity at 273 K η_0	10 ¹³ Pa s	<i>Barr and Showman</i> [2009]
Ice thermal conductivity k_i	567/ T W m ⁻¹ K ⁻¹	<i>Klinger</i> [1980]
Water thermal conductivity k_w	0.6 W m ⁻¹ K ⁻¹	
Ice specific heat C_i	2.11 kJ kg ⁻¹ K ⁻¹	
Water specific heat C_w	4.19 kJ kg ⁻¹ K ⁻¹	
Latent heat of fusion L_f	334 kJ kg ⁻¹	
Gravitational acceleration g	1.3 m s ⁻²	

^aTemperature independent over the relevant range of 110–260 K.

Ocean overpressures are calculated to be in the range of 10⁴ to 10⁶ Pa with the upper bound an estimate of the tensile strength of the ice shell [Manga and Wang, 2007]. Hence, at the depth of emplacement, the difference $\Delta P_0 - (\rho_w - \rho_i)gh_s$ is likely $\sim 10^4$ to $< 10^6$ Pa. In that case the emplacement velocity v_w of the intrusion is ~ 1 to < 40 m s⁻¹. This estimate is consistent with the value of a few meters per second obtained by Crawford and Stevenson [1988] for gas-driven vertical ascent of a crack.

For a 2-D geometry, the width w of the dike is determined by a balance of the overpressure holding it open and restoring elastic stresses [Rubin, 1995]

$$w = \Delta P_0 h_s (1 - \nu) / G, \quad (4)$$

where ν is Poisson's ratio and G is the shear modulus (Table 1). For overpressure values between 5×10^4 and 5×10^5 Pa, the dyke width w is between 0.1 and 1 m and the injection rate is likely to be 0.1 to less than ~ 10 m² s⁻¹. For an elongated dyke of 100 m to 1 km in length, this 2-D injection rate corresponds to a volumetric rate of ~ 10 to less than 10⁴ m³ s⁻¹.

3.2. Driving Pressure in a Shallow Versus a Deep Sill

At shallow depths, the sill volume is accommodated by lifting and bending the upper layer of ice, because its flexural rigidity is much smaller than that of the bottom layer (Figure 3a). To model sill intrusion at shallow depth, we thus assume that water intrudes above a rigid horizontal surface and below an elastic upper layer of flexural rigidity D_u given by

$$D_u = \frac{E d_u^3}{12(1 - \nu^2)}, \quad (5)$$

where E is Young's modulus, ν is Poisson's ratio, and d_u is the elastic thickness of the upper layer. In response to the applied pressure, the upper elastic layer deforms over a characteristic wavelength Λ_u equal to the flexural parameter [Turcotte and Schubert, 1982; Michaut, 2011; Lister et al., 2013]

$$\Lambda_u = \left[\frac{E d_u^3}{12(1 - \nu^2) \rho_w g} \right]^{1/4}. \quad (6)$$

The water pressure in the sill is the sum of the hydrostatic pressure due to the overlying ice and liquid water weight plus an elastic pressure generated by the deformation of the elastic upper layer. However, the lateral flow of water is driven by pressure gradients, and the hydrostatic pressure due to the overlying ice weight is constant everywhere, even beyond the sill. Hence, the dynamic pressure P available for lateral spreading of a shallow sill of water at the contact plane with the rigid basal boundary is simply the sum of the pressure at the top of the sill due to elastic deformation plus the pressure due to water weight

$$P(x, t)^{\text{shallow}} = D_u \frac{\partial^4 h(x, t)}{\partial x^4} + \rho_w g h(x, t), \quad (7)$$

where $h(x, t)$ is the flow thickness.

If a sill intrudes deep into the elastic part of the ice shell, the pressure necessary for lifting the overlying layer is larger than the pressure necessary for bending the lower layer and the sill makes room for itself preferentially by deforming the lower elastic layer. In the case of a deep sill, we thus assume that the sill intrudes below a rigid layer and above an elastic layer of thickness d_l , rigidity D_l , and flexural wavelength Λ_l , with D_l and Λ_l given by (5) and (6), where d_u has been replaced by d_l .

In this limit, the dynamic pressure available for sill spreading along the rigid bottom of the upper layer is only the pressure due to the elastic deformation of the lower layer. Pressure due to water weight does not contribute to sill spreading, as it acts in the opposite direction and balances the restoring force, equal in amplitude and opposite in direction, applied to the base of the lower deforming elastic layer due to water displacement in the ocean. Thus,

$$P(x, t)^{\text{deep}} = D_l \frac{\partial^4 h(x, t)}{\partial x^4}. \quad (8)$$

3.3. Shape of the Sill

Studies on the spreading of a viscous fluid driven by an elastic overlying layer have shown that the pressure gradient is small over the bulk of the flow and is largest at the ends of the flow [Flitton and King, 2004]. The elastic overlying layer acts to distribute the available pressure over the whole length of the layer, despite the finite viscosity of the fluid. For instance, for a newtonian fluid, the pressure gradient is equal to zero over the whole flow, except at the very tip [Michaut, 2011; Lister et al., 2013; Michaut et al., 2013; I. J. Hewitt et al., Elastic-plated gravity currents, submitted to *Journal of Applied Mathematics*, 2013], and fluid spreading occurs by peeling off the upper elastic layer at the top [Lister et al., 2013]. In that case, the pressure in the flow can be assumed constant. If gravity is involved as well, this assumption is valid up to a sill length of at least $\sim 10 \Lambda_u$, when gravity largely controls the flow. Pressure gradients are then no longer negligible over the flow length, and the flow is equivalent to a gravity current [Michaut, 2011; Lister et al., 2013; Thorey and Michaut, 2014; Hewitt et al., submitted manuscript, 2013].

To derive a simple expression for the flow morphology, for flow length up to at least $\sim 10 \Lambda_u$ for shallow sills and for any flow length for a deep sill, for which gravity is not involved, we assume, to first order, that the pressure available for intrusion varies with time but is uniform in x and solve

$$P(t)^{\text{shallow}} = \rho_w g h(x, t) + D_u \frac{\partial^4 h(x, t)}{\partial x^4} \quad (9)$$

to obtain the corresponding flow shape $h(x, t)$ for a shallow sill. The solution to (9), using appropriate boundary conditions $\left(\frac{\partial h}{\partial x}\right)_0 = 0$ and $h(L) = \left(\frac{\partial h}{\partial x}\right)_L = 0$, where L is the flow half-length, gives the flow shape $h(x, t)$ of a shallow sill as a function of the driving pressure $P(t)^{\text{shallow}}$:

$$h(x, t) = \frac{P(t)^{\text{shallow}}}{\rho_w g} \left[1 + \frac{Sc + Cs}{Sc(Ss - Cc) - Cs(Ss + Cc)} \cosh \frac{x}{\sqrt{2}\Lambda_u} \cos \frac{x}{\sqrt{2}\Lambda_u} - \frac{Sc - Cs}{Sc(Ss - Cc) - Cs(Ss + Cc)} \sinh \frac{x}{\sqrt{2}\Lambda_u} \sin \frac{x}{\sqrt{2}\Lambda_u} \right], \quad (10)$$

where

$$C = \cosh \frac{L(t)}{\sqrt{2}\Lambda_u} \quad c = \cos \frac{L(t)}{\sqrt{2}\Lambda_u} \quad S = \sinh \frac{L(t)}{\sqrt{2}\Lambda_u} \quad s = \sin \frac{L(t)}{\sqrt{2}\Lambda_u}.$$

For a constant injection rate, conservation of mass requires that

$$Q_0 t = \int_0^{L(t)} h(x, t) dx. \quad (11)$$

Introducing (10) into (11), we obtain

$$Q_0 t = \frac{P(t)^{\text{shallow}}}{\rho_w g} \left[L(t) + \sqrt{2}\Lambda_u \frac{Sc}{Sc(Ss - Cc) - Cs(Ss + Cc)} \cos \frac{L(t)}{\sqrt{2}\Lambda_u} \sinh \frac{L(t)}{\sqrt{2}\Lambda_u} + \sqrt{2}\Lambda_u \frac{Cs}{Sc(Ss - Cc) - Cs(Ss + Cc)} \cosh \frac{L(t)}{\sqrt{2}\Lambda_u} \sin \frac{L(t)}{\sqrt{2}\Lambda_u} \right], \quad (12)$$

which relates $P(t)$ to flow length L and time t .

The same analysis, but in the case of a deep sill, gives

$$P(t)^{\text{deep}} = D_l \frac{\partial^4 h(x, t)}{\partial x^4} \quad (13)$$

$$h(x, t) = \frac{P(t)^{\text{deep}}}{24D_l} L(t)^4 \left(1 - \frac{x^2}{L(t)^2} \right)^2 \quad (14)$$

$$Q_0 t = \frac{P(t)^{\text{deep}} L(t)^5}{45D_l}. \quad (15)$$

Calculations will show that these last equations (13) to (15), where D_l is replaced by D_u , also provide a good approximation for the shape and pressure evolution for a shallow sill when $L \ll 4\Lambda_u$, because the elastic pressure is then dominant over the weight of the flow. When $L \sim 4\Lambda_u$, pressure due to sill weight cannot be neglected and these approximations are no longer valid. Pressure gradient effects are investigated in Appendix C; the resulting flow shape is not significantly different from the uniform pressure solution.

As long as the pressure in the sill is large enough to allow for crack propagation, crack opening is not a limiting process and the sill should spread even if cooling and freezing occur at the tip, where the sill thickness reduces to zero. Injected water will continue to flow into and thicken the sill, and the elastic response of the layer causes water spreading. We show, in Appendix D, that advection of heat is larger than heat loss in most of the sill (> 90%) during the entire emplacement process, creating a thermal anomaly in the surrounding ice and allowing continued spreading of liquid water.

3.4. Spreading Phase

Because water viscosity is low, the inertial term is larger than the viscous term. The Reynolds number $Re = \frac{\rho_w H dL/dt}{\mu_w}$, with μ_w the water viscosity and H a characteristic thickness for the flow, is thus larger than 10^3 and the flow is turbulent; this will be verified a posteriori. Hence, as long as the pressure is large enough for fracturing to occur at the tip, the pressure necessary for bending the overlying layer is balanced by inertia; additionally, friction at the roof and bottom of the intrusion probably occurs and decreases the pressure available for spreading

$$P(t) = \frac{1}{2} \rho_w \left(\frac{dL}{dt} \right)^2 \left(1 + \frac{fL}{D_h(t)} \right), \quad (16)$$

where the second term on the right represents friction loss. We modify the expression for friction loss through a pipe to account for the 2-D geometry of the sill by using $D_h = 2h_0(t)$, where D_h is 4 times the central section area of a sill divided by its perimeter (with this definition for D_h , we recover the expression for a circular pipe flow) and $h_0(t)$ is the thickness at the sill center. Friction loss is given by f , the friction coefficient, and, for $Re > 10^3$, it is given by the Blasius equation [Turcotte and Schubert, 1982]

$$f = 0.31 Re_h^{-1/4} = 0.31 \left(\frac{\rho_w D_h dL}{\mu_w dt} \right)^{-1/4}, \quad (17)$$

where $Re_h = (\rho_w D_h dL/dt)/\mu_w$ is the modified Reynolds number for a 2-D flow with friction where we use again $D_h = 2h_0$.

In the case of a shallow sill, using $P(t)^{\text{shallow}}$ given by (12) in (16), we obtain a differential equation for the time evolution of the flow length $L(t)$ of a shallow sill

$$\frac{1}{2} \rho_w \left(\frac{dL}{dt} \right)^2 \left(1 + \frac{fL}{2h_0(t)} \right) = Q_0 t \rho_w g \left[L(t) + \sqrt{2} \Lambda_u \frac{Sc}{Sc(Ss - Cc) - Cc(Ss + Cc)} \cos \frac{L(t)}{\sqrt{2} \Lambda_u} \sinh \frac{L(t)}{\sqrt{2} \Lambda_u} + \sqrt{2} \Lambda_u \frac{Cs}{Sc(Ss - Cc) - Cc(Ss + Cc)} \cosh \frac{L(t)}{\sqrt{2} \Lambda_u} \sin \frac{L(t)}{\sqrt{2} \Lambda_u} \right]^{-1}. \quad (18)$$

In the case of a deep sill, using $P(t)^{\text{deep}}$ given by (12) in (16), we have

$$\frac{1}{2} \rho_w \left(\frac{dL}{dt} \right)^2 \left(1 + \frac{fL}{2h_0(t)} \right) = \frac{Q_0 t 45 D_l}{L(t)^5}. \quad (19)$$

Both equations, which neglect the influence of a pressure gradient within the bulk of the flow, are solved numerically using a fourth-order Runge-Kutta scheme. The effects of a pressure gradient within the bulk of the flow are investigated in Appendix C; the resulting flow evolution is close to the one we obtain here using the assumption of a uniform pressure because pressure gradients are concentrated near the sill ends.

In the case where friction is neglected, i.e., $f = 0$ in (16), we obtain an instructive analytical solution for the evolution of a deep sill morphology with time by introducing the expression for $P(t)$ given by (15) in (16) with $f = 0$ and integrating

$$L(t) = \left(\frac{7}{3}\right)^{2/7} \left(\frac{90D_l Q_0}{\rho_w}\right)^{1/7} t^{3/7}. \quad (20)$$

Then, using (20) in (14) and (15), we obtain

$$h_0(t) = \frac{15}{8} \left(\frac{3}{7}\right)^{2/7} Q_0^{6/7} \left(\frac{\rho_w}{90D_l}\right)^{1/7} t^{4/7}, \quad (21)$$

$$h_0(L) = \frac{15}{8} \left(\frac{3Q_0}{7}\right)^{2/3} \left(\frac{\rho_w}{90D_l}\right)^{1/3} L^{4/3}. \quad (22)$$

The scaling law given by (22) shows that the thickness in the sill center will increase with the injection rate Q_0 because the applied pressure on the elastic plate is then larger; see equations (15) as well as (12). Furthermore, the smaller the elastic layer rigidity, the thicker the sill is because the resistance to bending is then smaller.

During the spreading of a deep sill and the initial spreading phase of a shallow sill, where bending is dominant, the scaling laws provided by (21) and (22) parallel the thickness-to-length and thickness-to-time evolution calculated numerically when friction and gravity are accounted for, because the elastic pressure is then the dominant term for sill spreading. The effect of friction loss is to increase the sill thickness by decreasing the pressure available for bending and peeling off the elastic layer at the tip (Figure 4). When L reaches $4\Lambda_v$, gravity is no longer negligible and increases the pressure available for, and hence promotes, spreading at the expense of thickening for a shallow sill (blue lines in Figure 4). Increasing the injection rate leads to an increase in the thickness at a given length as predicted by (22), but, for realistic parameter values, the maximum thickness that can be reached in the case of a shallow sill is at most a few meters because water weight promotes sill spreading (Figure 4). On the contrary, for a deep sill, because water weight does not play a role, the sill continues to thicken (Figure 4).

Equation (20) implies a spreading rate

$$\frac{dL}{dt} = \left(\frac{3}{7}\right)^{5/7} \left(\frac{90D_l Q_0}{\rho_w}\right)^{1/7} t^{-4/7}. \quad (23)$$

For an elastic thickness $d_l = 100$ m, an injection rate $Q_0 = 0.5 \text{ m}^2 \text{ s}^{-1}$, and using values for the parameter listed in Table 1, we calculate that the tip velocity decreases from ~ 34 to 0.2 m s^{-1} from $t = 1 \text{ s}$ to $t = 10^4 \text{ s}$. Hence, given the low viscosity of liquid water, we verify that the Reynolds number is $\gg 1$ even for very small flow thicknesses of ~ 1 mm, characteristic of the tip.

3.5. Fracture Toughness Limit

As the flow length increases, the pressure in the sill eventually decreases to the critical value equal to the pressure necessary for fracturing at the tip, P_f . In that case fracturing at the tip might limit sill spreading. The stress intensity factor K_I for a mode I fracture and a uniformly loaded crack situated close to a boundary (i.e., $d \ll L$) can be approximated by [Dyskin *et al.*, 2000]

$$K_I = K_M M_0 d^{-3/2}, \quad (24)$$

where K_M is a constant equal to 1.951 [Dyskin *et al.*, 2000] and M_0 is the moment about the crack tip given by

$$M_0 = \frac{Ed^3}{12(1-\nu^2)} \left(\frac{\partial^2 h}{\partial x^2}\right)_{x=L(t)}, \quad (25)$$

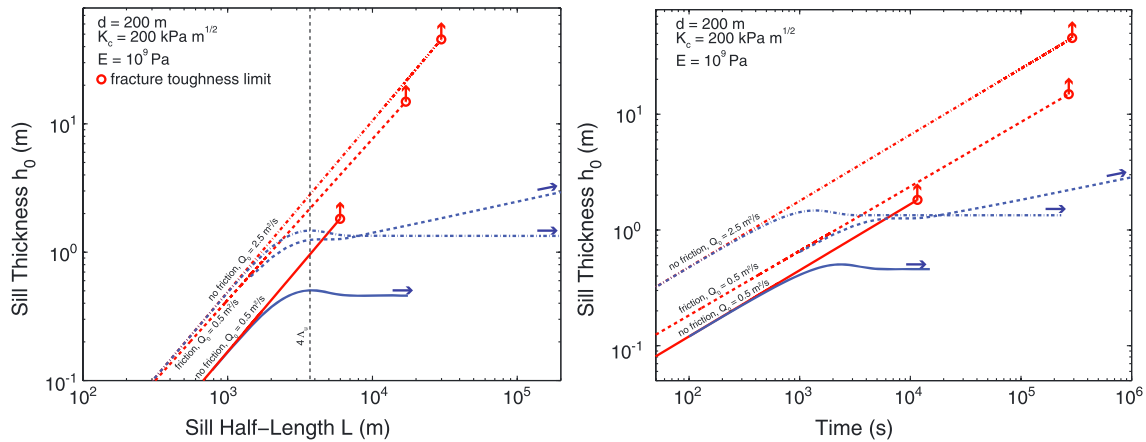


Figure 4. Evolution of the maximum thickness (i.e., thickness at the center) as a function of (left) sill half-length and (right) time for a spreading sill of water at shallow depth (blue lines) and deep depth (red lines) for different values of the injection rate Q_0 , accounting or not for friction. When the sill half-length is less than $4\Lambda_u$, gravity is negligible and the scaling laws provided by (21) and (22), red solid line and red dash-dotted line, well represent the evolution of the sill morphology when friction is neglected, even for shallow sills. When L reaches $4\Lambda_u$, gravity is no longer negligible and increases the pressure available for, and hence promotes, spreading at the expense of thickening. As a result, the critical pressure at which the stress intensity factor becomes equal to the ice fracture toughness limits the lateral extent of deep sill (red circles), allowing for sill thickening (red arrows), while it does not in the case of shallow sills, which continue to spread.

which increases with the internal sill pressure. Once K_I reaches the fracture toughness limit K_c , i.e., once the pressure in the sill decreases to a critical pressure such that $K_I = K_c$, fracturing at the tip limits the sill's lateral extent. Since freezing is fastest at the tip ($h \rightarrow 0$), the crack should close, impeding further sill spreading. Appendix D shows that the hot thermal anomaly due to injection of water extends at least over nine-tenths the length of the sill during the entire spreading phase and hence that cooling and freezing at the tip should not limit propagation during the spreading phase. However, the extent of the cooling front, which is between one twentieth and one tenth of the sill extent, is probably large enough for a deep sill that when the fracture toughness limit is reached, water near the sill tip will freeze shut the sill.

Using the expression for $h(x, t)$ as a function of length $L(t)$ and pressure $P(t)$ for a shallow sill given by (14) in (25) and (24), we find the critical pressure at which fracturing limits sill propagation

$$P_c(t)^{\text{shallow}} = \frac{K_c}{1.951} \frac{d_u^{3/2}}{\Lambda_u^2} \left(-\frac{Cs + Sc}{Sc(Ss - Cc) - Cs(Ss + Cc)} \sinh \frac{L(t)}{\sqrt{2}\Lambda_u} \sin \frac{L(t)}{\sqrt{2}\Lambda_u} + \frac{Cs - Sc}{Sc(Ss - Cc) - Cs(Ss + Cc)} \cosh \frac{L(t)}{\sqrt{2}\Lambda_u} \cos \frac{L(t)}{\sqrt{2}\Lambda_u} \right). \quad (26)$$

And, in the case of a deep sill, using (14) in (25) and (24), we have

$$P_c(t)^{\text{deep}} = \frac{3K_c}{1.951} \frac{d_l^{3/2}}{L(t)^2}. \quad (27)$$

The critical length L_c at which the stress intensity factor equals the fracture toughness of ice is then obtained when the sill's internal pressure $P(t)^{\text{shallow}}$ or $P(t)^{\text{deep}}$ becomes equal to P_c . For a deep sill, when friction is neglected, we obtain an analytical expression for L_c

$$L_c = d^{3/4} \left(\frac{15K_M}{K_c} \right)^{3/2} \frac{3Q_0}{7} \left(\frac{\rho_w E^2}{90 \times 12^2 (1 - \nu^2)^2} \right)^{1/2}. \quad (28)$$

Equation (28) shows that this critical sill length increases with the injection rate Q_0 because the pressure available for spreading increases. L_c is also strongly controlled by the fracture toughness K_c : larger values of K_c lead to shorter sill lengths. The value of K_c for ice is well constrained by experiments for the range of temperature and pressure applicable to Europa's ice shell, between 100 and 300 $\text{kPa m}^{-1/2}$ [Liu and Miller, 1979; Litwin et al., 2012]. However, distributed inelastic deformation in the stressed elastic layer could significantly increase this value and hence decrease the critical sill length at which sill spreading stops.

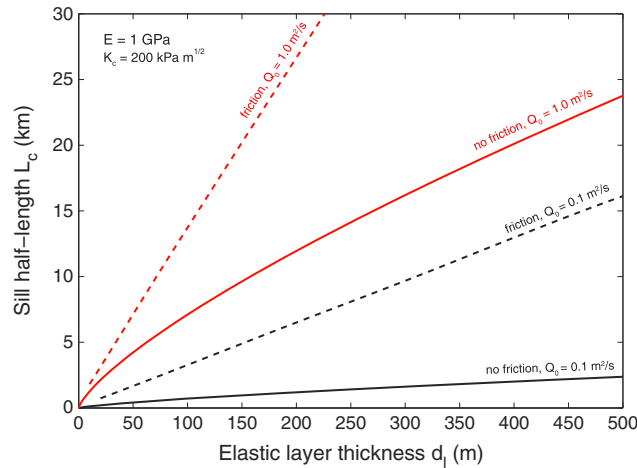


Figure 5. Critical sill length L_c when the fracture toughness limit is reached, as a function of the elastic layer thickness d_l of the underlying layer, for two different injection rates and with or without friction; friction coefficient f given by (17) or $f = 0$.

Calculations show that the fracture toughness limit is reached for shallow sills only if the injection rate Q_0 is in the lowest possible range of values, i.e., $\leq 0.2 \text{ m}^2 \text{ s}^{-1}$. Above this limit, gravity promotes spreading and promotes fracturing at the tip (Figure 4). On the contrary, for deep sills, the fracture toughness limit is reached at a critical length between a few to a few tens of kilometers (Figures 4 and 5), depending on the injection rate and elastic layer thickness. The critical sill length L_c increases significantly if friction is accounted for (Figures 4 and 5). Indeed, when friction matters, the sill is thicker for a given length and the sill length must increase for the moment at the tip M_0 , which scales as h_0/L^2 (25), to decrease to the value such that $K_f = K_c$.

When this critical length is reached, the sill does not spread further because the crack is closed by freezing, and the sill can thicken by further injection of water. Eventually, if the pressure in the sill increases to a value that permits renewed fracturing, elastic stresses in the overlying and underlying elastic layers would favor upward or downward propagation, possibly creating saucer-shaped sills.

The emplacement of a sill by downward flexure of the lower elastic layer is particularly appealing in the case of icy satellites, and hence Europa, for mechanical reasons. Water ascent in the ice shell will consume most of the initial water overpressure, since liquid water buoyancy is negative in the ice shell. For instance, for an initial overpressure in the water source of 10^5 Pa , the dyke can only ascend through $\sim 1 \text{ km}$ of ice. Since large overpressure values may be difficult to achieve in the liquid ocean (Manga and Wang, 2007), a deep intrusion seems more reasonable. Furthermore, thickening of the sill by upward deflection of the upper elastic layer is limited: as shown above, water weight acts against thickening and favors sill spreading and fracturing at the tip. In contrast, thickening of a deep sill can occur because water weight does not contribute to the pressure acting in favor of sill spreading and fracturing so that fracturing limits the lateral extent of deep sill. Finally, downward flexure of the lower elastic layer provides a way of keeping the pressure high in the ocean, enhancing water intrusion. Indeed, if the intrusion is deep, the water volume is transferred to the ice shell without a significant increase in the total volume of the water plus ice layer: the only increase in volume which could help release the ocean overpressure comes from the upward deflection of the upper layer, which is negligible compared to the total volume of the sill. Thus, large volumes of water could be intruded deep into the elastic part of the ice shell. In contrast, for shallow sills, water overpressure is not only partially compensated by the water weight but is also rapidly depleted since the volume of water transferred to the sill is accommodated by uplift of the overlying layer.

4. The End of Sill Intrusion: Dyke Solidification

As water intrudes the ice shell through a dyke, it heats the surrounding ice as it cools and solidifies. Thermal boundary layers develop in the ice and water and grow with time until cooling and solidification closes the dyke. We apply the model of Rubin [1993, 1995] for dykes of magma propagating within rocks and freezing at a unique temperature to the case of a liquid water dyke propagating vertically into the ice shell to deduce the timescale for dyke solidification and final sill volume. Rubin [1993, 1995] established that the frozen margin thickness δ_m grows with time as

$$\delta_m = 2\Theta\sqrt{\kappa t}, \quad (29)$$

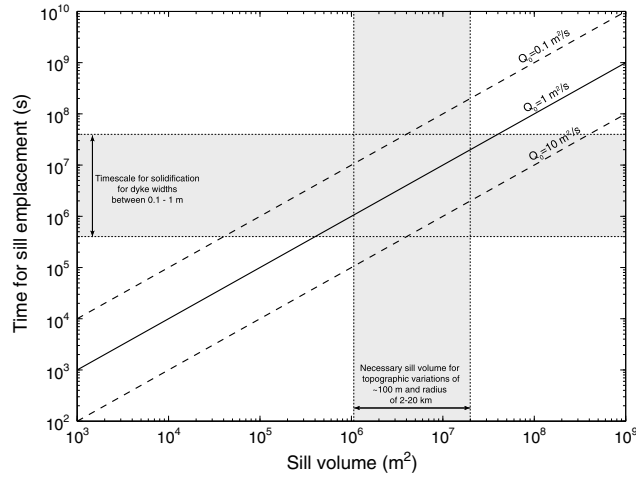


Figure 6. Timescale for sill emplacement as a function of sill volume for three different values of the injection rate, 0.1, 1, and $10 \text{ m}^2 \text{ s}^{-1}$. Also indicated are the timescale for dyke solidification and closing for dyke widths between 0.1 and 1 m [Rubin, 1993, 1995] and the volume of water necessary to produce topographic variations of order 100 m at the surface; see section 5. Compatible injection rates are between 0.1 and $10 \text{ m}^2 \text{ s}^{-1}$, corresponding to overpressure values in the water source of $>10^4$ to $<10^6$ Pa.

ice. Using values for the parameters listed in Table 1, we calculate a timescale for dyke arrest by solidification equal to the timescale necessary for the frozen margin thickness to reach the dyke width; this timescale is between 4×10^5 and 4×10^7 s for dyke widths between 10 cm and 1 m as calculated in section 3.1.

For injection rates between 0.1 and $10 \text{ m}^2 \text{ s}^{-1}$, dyke widths between 10 cm and 1 m allow for intrusion of a water volume (per unit length) of 10^5 to 10^8 m^2 (Figure 6). In section 5, we conclude that the 2-D volume of water necessary to produce topographic variations of the order of 100 m at the surface is about 10^6 m^2 or more for sill half-length of several kilometers upon emplacement, which is compatible with estimated injection rate and timescale for water injection (Figure 6).

5. Evolution of the Water Body and Intrusion

Once the sill stops spreading, the subsequent evolution of its morphology and surface expression depend on the timescale of solidification and on the mechanical behavior of the ice shell. In this section we assess the consequences of solidification of the ice and how the excess weight of the water is compensated before it freezes completely.

5.1. Deformation of the Base of the Ice Shell

Intrusion of a deep sill deflects downward the base of the ice shell. The topography at this ice-water interface will relax by viscous flow. The timescale for this relaxation was addressed by Nimmo [2004] and is not rederived here. For ice with the temperature structure given in Appendix A, the timescale for relaxation by Newtonian creep is

$$\tau_{\text{relax}} = \frac{\eta_0 \lambda^2}{4(\rho_w - \rho_i)g\delta^3 \pi^2} \quad \delta = RT_b t_c / Q \ln(T_b / T_s), \quad (31)$$

where $\delta = RT_b t_c / Q^* \ln(T_b / T_s)$ is the length scale over which viscosity changes by a factor of e , T_b and T_s are the bottom and surface temperatures of the ice shell, Q^* is the activation energy, R is the gas constant, t_c is the shell thickness, and λ is the wavelength of the deformation which we take as the lateral extent of the sill.

τ_{relax} is less than a few hundred years, i.e., less than 10^{10} s, for viscosities at the base of the ice shell less than 10^{14} Pa s.

As we show next, relaxation of topography and sill intrusion both occur on timescales much shorter than the time to solidify the intruded water.

where the thermal diffusivity of water κ is given by $\kappa = k_w / \rho_w C_w$ with k_w the thermal conductivity and C_w the heat capacity and where Θ depends on C_w as well as on liquid water and ice temperature T_w and T_i and latent heat of fusion of ice L_f

$$\Theta = \frac{C_w(T_w - T_i)}{\sqrt{\pi} L_f}. \quad (30)$$

For an ice shell and ocean at thermal equilibrium, the liquid water temperature is between 269 and 273 K [Ruiz, 2010] and the temperature in the ice shell at the equator varies from 110 K at the surface to the ocean temperature at the shell bottom, with an average of 163 K. Since we suppose the sill intrudes relatively deep into the ice shell, we use an average temperature difference of 60 K between the liquid water and the surrounding

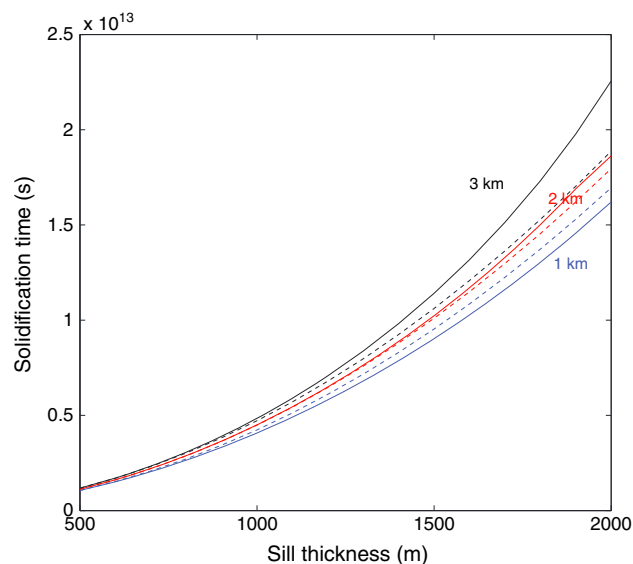


Figure 7. Solidification time τ_{solidify} as a function of sill thickness, for sills whose upper surfaces are at depths of 1, 2, and 3 km. Thermal parameters are summarized in Table 1. The dashed curves show a thickness-squared scaling for these three depths, calibrated to the solidification time of the thinnest 500 m sill.

(assuming the water is not superheated) because cooling and solidification are limited by heat loss to the surroundings [Marsh, 1989; Worster et al., 1990]. We account for the possible convection of water in the sill by assuming a constant temperature within the liquid part of the sill.

Figure 7 shows the cooling times for sills 500 m to 2 km thick intruded into a 10 km ice shell so that their upper surfaces are at depths of 1, 2, or 3 km. If the sill has a thickness comparable to or thinner than its emplacement depth, the solidification time is dominated by its thickness and emplacement depth has little effect. As the sill thickness increases, the solidification time increases roughly quadratically, as expected for a diffusion problem in an infinite domain. The black dashed curves show a thickness-squared solidification time, normalized by the solidification time for the 500 m sill. The effect of a finite layer above the sill, and cooling to the underlying ice modify the solution somewhat from the infinite space solidification problem, with the former leading to faster solidification.

For the range of sill depths and thicknesses we would require to explain pits and domes, solidification times are expected to be in the range 1×10^{12} to 3×10^{13} s. We thus verify that this is indeed much longer than the estimated emplacement times (Figure 6). In addition, the solidification time is much longer than the timescale for topography at the base of the ice shell to relax; see section 5.1.

5.3. Flexural Support of the Sill Before it Solidifies

An important consequence of heat transfer is that the elastic layers above and below the sill will become thinner and thus stresses will be enhanced above the sill. Regional and global stresses on Europa are large enough to create tectonic features such as bands and ridges, and so we expect that stresses are in general close to those needed for failure. Large stresses in the ice shell are a natural consequence of its formation: cooling of ice and volume changes upon freezing generate tension near the surface and compression at greater depths [Nimmo, 2004]. If the sill originated from an overpressured ocean, we also expect large pre-existing stresses in the ice shell [Manga and Wang, 2007]. The local thinning of the part of the ice shell able to support elastic stresses will increase the magnitude of those stresses. Even though the ice above the sill is warm, cracks formed at shallower depths will still be able to penetrate to depths of a few kilometers and through this warm ice because the ice will behave elastically on the timescale for crack formation [Rudolph and Manga, 2009]. We assume, for now, that stress concentrations become large enough to disrupt the layer of ice above the sill and that this layer is strengthless. Any overpressure in the sill will dissipate at this point, and the disrupted ice will float on top of water in the sill.

5.2. Timescale for Sill Solidification

We assume that cooling is governed by vertical heat conduction from the sill to both the overlying and underlying colder ice

$$\frac{\partial T}{\partial t} = \frac{1}{\rho_i C_i} \frac{\partial}{\partial z} \left(k_i(T) \frac{\partial T}{\partial z} \right), \quad (32)$$

where ρ_i and C_i are the density and specific heat of ice, respectively. The latent heat of water will slow cooling. We account for the latent heat by using an equivalent specific heat spread over a 1° temperature range [Mottaghy and Rath, 2006]. We define the solidification time τ_{solidify} as the time it takes to cool the water sill to below its freezing temperature everywhere. Owing to the nonlinearity of k_i (Table 1), we solve (32) numerically using an explicit finite difference method. Convection may occur within the water sill but will not significantly affect the solidification time

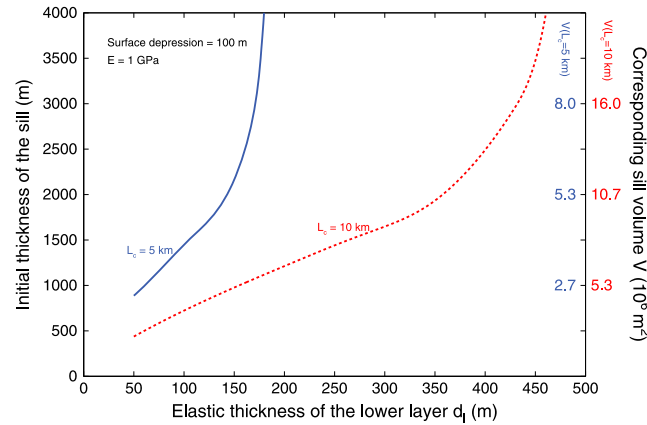


Figure 8. Sill thickness and corresponding volume required (at the end of intrusion) to arrive at a surface depression equal to 100 m as a function of elastic thickness of the bottom layer d_l for two different sill half-lengths of 5 and 10 km. The two volume scales on the right correspond to the two different sill half-lengths.

Because the weight of the sill is no longer compensated by a thickened ice shell (section 5.1), the additional weight of water relative to ice is compensated by downward flexure of the lower elastic layer, whose thickness is reduced owing to heat transfer from the overlying ice (Figure 2, stages 3 and 4).

Downward flexure of the ice shell should satisfy (Figure 2, stages 3 and 4)

$$D_l \frac{\partial^4 h_f(x)}{\partial x^4} = (\rho_w - \rho_i)gh_f(x) - \rho_w gh_f(x_b) \quad \text{for } 0 < x \leq x_b \quad (33)$$

$$D_l \frac{\partial^4 h_f(x)}{\partial x^4} = -\rho_i gh_f(x) \quad \text{for } x_b \leq x < L_c \quad (34)$$

where $h_f(x)$ is the (downward) displacement of the lower elastic layer, and x_b is the new sill length (as the lower layer bends, the sill thickens and shortens). The downward displacement of the elastic layer is large enough to accommodate the total weight of liquid equal to $\rho_w \int_{-L_c}^{L_c} h_0(x)dx$ and induces a surface depression. Since the upper layer is now assumed to be strengthless, the liquid water surface is flat and at a depth $z = -h_f(x_b)$, which corresponds to the observed depression at the surface.

In addition, the mass of water is conserved

$$\int_0^{x_b} (h_f(x) - h_f(x_b))dx = \int_0^{L_c} h(x)dx = \frac{8}{15} h_0 L_c, \quad (35)$$

where we assume that the sill retains its bell shape by elastically deforming the underlying layer while it thickens after the fracture toughness limit is reached.

For given values of the sill length L_c , flexural rigidity D_l and surface depression $h_f(x_b)$, we numerically solve (33) to (35) to find, by iteration on x_b , the pair of solutions (x_b, h_0) . The initial maximum thickness of water and corresponding volume given by (35) required to create a 100 m depression at the surface increases with the elastic thickness of the lower layer d_l (Figure 8).

Compensation acts to decrease the aspect ratio (length/thickness) of the water body. After compensation, the sill changes shape and its apparent radius might decrease significantly, in particular if d_l is small and the sill volume is large. We take two different examples, both leading to a depression of 100 m at the surface and characterized by two different sill lengths, $L_c = 5$ and 10 km, and volumes, $V = 3.0 \times 10^6 \text{ m}^3$ and $5.6 \times 10^6 \text{ m}^3$, and two different elastic thicknesses for the underlying layer, $d_l = 72$ and 170 m, respectively; these two cases could, for instance, correspond to intrusion of water at a rate of $\sim 1 \text{ m}^2 \text{ s}^{-1}$ (Figure 5, no friction) if no thinning by heating of the underlying elastic layer has occurred in between sill emplacement and compensation. For these examples, the final sill lengths after compensation x_b are, respectively, 2.7 km and 5.2 km. Because water weight is now concentrated over approximately two thirds of the layer, the large downward central flexure of the elastic layer is accommodated by an adjacent upraised annulus 32 m high. The apparent half-length of the resulting pit structure at the surface is only about two thirds of the initial half-length (Figure 9). The surface topography is relatively flat within the pit, though the actual surface topography will differ somewhat from that shown in Figure 9 because the overlying ice layer is considered strengthless in the calculation.

Thus, compensation of liquid water emplaced as a sill into the ice shell can induce pit formation at the surface, with a negative relief of 100 m or more, if the sill emplacement depth is within, though deep into, the elastic part of the ice shell. For typical timescales necessary for sill emplacement, which allow for injection of less than $\sim 10^7 \text{ m}^3$ of water, the elastic thickness of the bottom layer at the time of compensation must be less than ~ 200 m, for initial sill half-lengths of 5 to 10 km and initial thicknesses of the order of a kilometer. The final apparent radius of the pit at the surface would then be between 3 and 6 km (Figure 9).

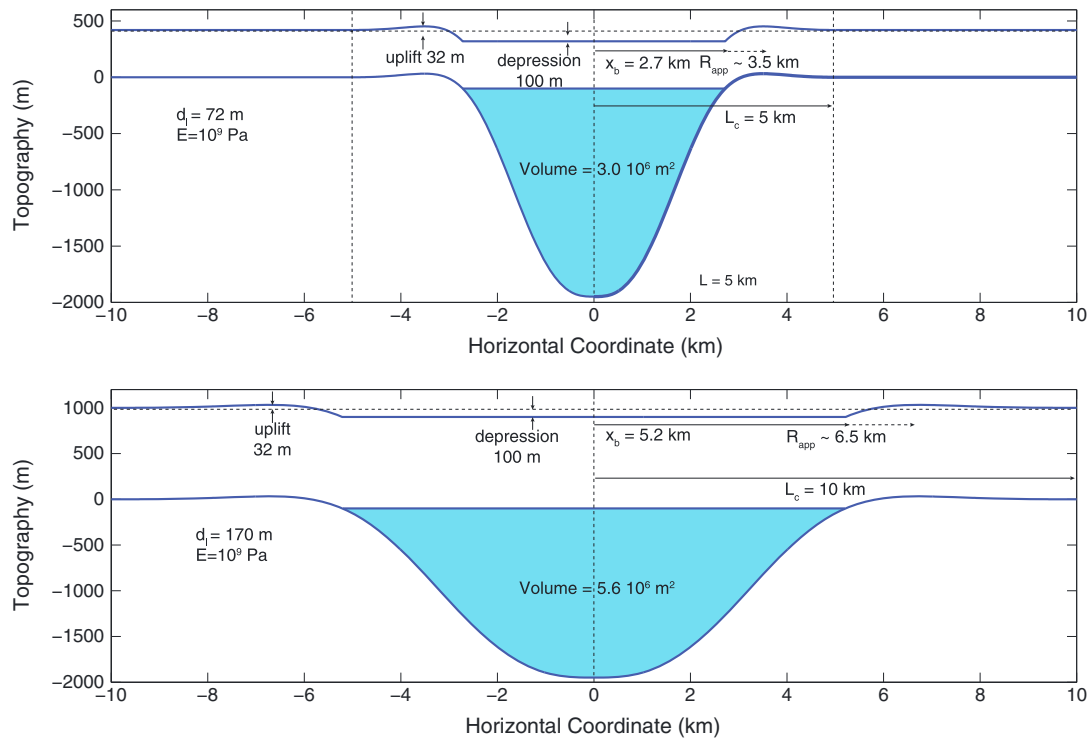


Figure 9. Shape of the sill after compensation in two different cases (two different elastic thicknesses, d_i , two different initial half-lengths $L_c = 5$ or 10 km and volumes, indicated on the figures), both leading to a surface depression of 100 m. For the sake of illustration, an upper layer with thickness $d_u = 10d_i$ is represented on top of the sill. The zone filled with water is blue.

5.4. Diapiric Descent of the Sill

If the ice underneath the sill is heated to the point that it can no longer provide elastic support for the weight of the sill, the water will sink through the underlying viscous ice as a diapir. Owing to the low viscosity of water relative to ice, stability analysis indicates that a single diapir will form [Whitehead and Luther, 1975]. The timescale to create a diapir from a sill-shaped body can be estimated from the analogous problem of a spreading low-viscosity diapir as a gravity current—an appropriate geometry because the lateral dimension of the sill L_c is much greater than its thickness h_0 . The problems are analogous geometrically, but the driving forces are in the opposite direction; owing to the reversibility of creeping flows, for a given geometry the sign of the velocities can simply be reversed in the solution. The long-term, large-deformation evolution will not be reversible, however, because the free boundary between the water and ice introduces a nonlinearity through the boundary conditions. For small deformations, however, the spreading and thickening problems are analogous except for a sign change in the velocity.

Griffiths and Campbell [1991] found, using scaled laboratory experiments, that for a low-viscosity diapir ($\eta_w \ll \eta_i$) spreading below a rigid boundary (appropriate when the overlying ice remains elastic),

$$h(t) = (0.96 \pm 0.11)V_r^{1/3} \left[\frac{\Delta\rho g V_r^{1/3}}{\eta_i} t \right]^{-0.48 \pm 0.03}, \quad (36)$$

where V_r is the 3-D volume of the sill (in m^3). This empirical scaling is consistent with expected scaling and numerical results [Koch and Koch, 1995].

The time t_{diapir} for h to increase by a factor of 2, for example, will thus be

$$t_{\text{diapir}} = \frac{0.92\eta_i V_r^{0.36}}{\Delta\rho g} \left[\left(\frac{1}{h_0} \right)^{2.08} - \left(\frac{1}{2h_0} \right)^{2.08} \right]. \quad (37)$$

For illustrative purposes we consider a sill with $h_0 = 1000$ m, $L_c = 10$ km, a cylindrical geometry, and a volume $\pi h_0 L_c^2 / 4$. The time for h to increase by a factor of 2 is $2.9 \times 10^{-5} \text{ Pa}^{-1} \eta_i$. To obtain less deformation within the upper range of solidification times 3×10^{13} s (solidification removes the buoyancy driving

diapirism) requires viscosities $>10^{18}$ Pa s, corresponding to temperatures <190 K for the rheological parameters in Table 1. The viscosity structure in the ice underlying the sill is strongly depth dependent and time-evolving as heat is lost from the sill. However, temperatures warmer than 190 K are plausible. Thus, provided that all the underlying ice is warmed to the point that none of it can provide flexural support over solidification timescales, corresponding to temperatures less than 150 K for the largest sills, the sill may form a diapir and descend partially or completely to the ocean before complete water solidification.

5.5. Consequences of Water Freezing and Disruption of Ice

During solidification, the sill volume increases because of the lower density of ice compared to that of the liquid water. If the layer of ice above the sill has been disrupted, the expansion of ice freezing in the sill will be accommodated by a combination of water being expelled into cracks and other pore space within the disrupted ice and increasing the sill thickness.

We return to the initial 2-D geometry. The total volume (in m^2) of intruded liquid water is $V = \frac{8}{15}h_0L_c$, where h_0 and L_c were the sill initial thickness and length upon emplacement. Upon cooling, the volume of the intruded water increases by an additional volume ΔV and the depressed surface is uplifted by Δh^{up} :

$$\Delta V = \frac{\rho_i - \rho_w}{\rho_i} V = \frac{8}{9 \times 15} h_0 L_c = \frac{8}{15} \Delta h^{up} x_b. \quad (38)$$

We examine the two examples considered in section 5.3 where topographic relaxation at the base of the ice shell was complete and sill weight is compensated by downward flexure of the lower layer. After compensation, for a surface depression of 100 m, the sill thickness is 1849 m both for half-lengths x_b of 2.7 to 5.2 km (corresponding to initial sill half-lengths after emplacement of 5 and 10 km, respectively, and a lower layer elastic thickness of 72 and 170 m, respectively). In the first case (initial half-length of 5 km before compensation above a 72 m thick elastic layer), the total volume of the sill is $3.0 \times 10^6 \text{ m}^2$ corresponding to an initial sill thickness of ~ 1100 m, while in the second case (initial half-length of 10 km above a 170 m thick elastic layer), the total volume is $5.6 \times 10^6 \text{ m}^2$ corresponding to an initial sill thickness of ~ 1050 m. Hence, the additional volume after expansion is, respectively, 3.3×10^5 and $6.2 \times 10^5 \text{ m}^2$; it is accommodated by uplift of the overlying layer with a maximum of 220 to 230 m, i.e., a maximum topography of 120–130 m above 0, since the initial water level was depressed by 100 m relative to its initial emplacement depth.

If topographic relaxation of the water sill has not occurred at the base of the ice shell, then the additional weight of water is not flexurally compensated. Cooling and solidification of the sill leads to a volume increase of the sill and surface uplift. The additional volume caused by water solidification is still given by (38) and would result in a final uplift or final topography of 115 to 125 m above zero in the cases examined above (initial sill half-lengths of 5 km and 10 km). However, in this case, there is no pit stage.

6. Discussion

A successful model should explain several features of pits, domes, and small chaos. We list these observations and then address each in turn, identifying both successes and limitations of sills in accounting for the observations.

1. Diameters are typically ~ 3 –15 km with regional means in the range of about 3–6 km [Singer *et al.*, 2010]; some can be a few tens of kilometers in diameter [Schmidt *et al.*, 2004].
2. Pits and domes are sometimes associated with chaos and resurfacing to cover preexisting features.
3. There are more pits than domes [Singer *et al.*, 2010].
4. Relief is up to a few hundred meters [Schmidt *et al.*, 2004], with the mean relief between about 100 and 130 m [Singer *et al.*, 2010].
5. Relief increases as diameter increases [Singer *et al.*, 2010].
6. Pits and domes are among the younger features on the surface as they are rarely disrupted by other tectonic features [Pappalardo *et al.*, 1998].
7. Pits and domes are generally, though not always, constrained by apparent faults and ridges.

6.1. Diameters

The lateral dimensions of pits and domes are consistent with sills emplaced deep in the ice shell. If sills are in fact the origin of these features, the lateral dimensions are controlled by the mechanical properties of ice rather than dimensions of convective features in the ice shell [Pappalardo *et al.*, 1998; Nimmo and

Manga, 2002; Showman and Han, 2004] or plumes in the ocean [Thomson and Delaney, 2001; Greenberg et al., 2002]. If the water source is associated with rising diapirs in the ice shell [Schmidt et al., 2011], the location and spacing of pits and domes may still be controlled by solid state convection. The lateral dimensions of the pits are also controlled by the elastic thickness of the lower layer below the sill but are between about 2/3 and 1 times the initial sill length. Because domes are generated by expansion of water following the pit/compensation stage, the model predicts similar lateral dimensions for the pits and domes.

The origin of the water that makes sills in our model is not specified, only that there must be a source of overpressured water. The formation of a water sill at a depth of a few kilometers into the ice shell implies overpressures of one to several times 10^5 Pa in order for the water to ascend through one to several kilometers of ice. Upper values in this range of overpressures are larger than those predicted to develop in the ocean by cooling and freezing of the ice shell, assuming overpressure is limited by tensile stresses reaching the tensile strength of ice anywhere in the ice shell [Manga and Wang, 2007], though in the absence of failure, tensile stresses can get much larger than the tensile strength of ice [Nimmo, 2004]. Alternatively, buoyancy from gas exsolution may allow water to rise further into the ice shell [Crawford and Stevenson, 1988] and these gases would separate from the water once the sill is emplaced. Freezing of isolated water bodies [Fagents, 2003], including water generated in or above diapirs [Sotin et al., 2002; Pappalardo and Barr, 2004; Schmidt et al., 2011], should be able to produce overpressures up to values comparable to the tensile strength of ice, about $1 - 3 \times 10^6$ Pa [Schulson, 2006], and hence large enough to make the hypothesized sills. However, the water reservoir must also be large enough to supply enough water while maintaining a high pressure.

6.2. Formation of Small Chaos

Schmidt et al. [2011] explain how the disruption of ice above lenses of water could explain many, if not most, of the features of small chaos tabulated by Collins and Nimmo [2009], even though they did not estimate the thermal viability of their proposed eutectic melting model. Readers are referred to their analysis and discussion.

6.3. More Pits Than Domes

In our proposed model, pits indicate the presence of liquid water at depth. The final stage in the model is an uplifted topography following solidification of the intruded water. Given that the water stage has a finite lifetime, and domes may last forever, we might expect to see more domes than pits. A greater number of pits would thus imply that the formation of these features is recent and ongoing.

6.4. Relief

Relief of $\sim 10^2$ m implies sill thicknesses of $\sim 10^3$ m. Such thick sills, for diameters of a few km to 10 km, could form at relatively large depths in the ice shell, above a layer of ice with an elastic thickness of less than a few hundred meters.

The expected scaling of relief with diameter is complicated because, during the compensation stage, the radius of compensation x_b , as well as the apparent radius at the surface decreases relative to the initial sill length, in a way that depends on the total sill volume and elastic layer thickness (and ice viscosity if a diapir forms). Hence, the apparent radius at the surface may become similar for different initial sill lengths. However, the critical length L_c increases with the injection rate, and this should also be the case for the total sill volume, since large sill volumes imply larger timescales for sill emplacement and hence larger dykes and larger injection rates; thus, we expect the apparent relief at the surface to increase with increasing injection rate and diameter.

6.5. Age

If the water source is ocean water, the thicker the shell, the more overpressure in the ocean. If the water originates from diapirs in the ice shell, thicker ice may be needed for convection. Sills are thus more likely to form when the shell is thickest.

6.6. Interaction With Other Features

If a fault or a ridge affects the whole elastic lithosphere down to the emplacement level of the water sill, then the propagation of the sill might be stopped by such a fault. Indeed, a large pressure is then required to start a new crack and allow further propagation. The pressure might be sufficiently large only if the sill is still in the spreading regime and has not spread very far. Hence, large ridges and faults should generally

limit sill propagation and the resulting surface features such as depressions, domes, and small chaos should be generally constrained by large ridges and faults.

7. Summary

Our objective was to explore some of the mechanical and thermal constraints of the emplacement of water sills inside Europa's ice shell. We do find that water sills would have dimensions similar to those of pits and domes and could produce the observed relief. Whether there is a plausible source of the needed overpressure and volume of water is unclear (and was not modeled in the present study). The hypothesis is testable with radar, and we predict that pits should be located above bodies of liquid water, as does *Schmidt et al.* [2011]. These sills are likely to be located at depths of a few to several kilometers, depending on the total thickness of the ice shell. Provided that ocean pressure is large enough or gases can exsolve from the ascending water, the emplacement of sills provides a mechanism to transfer large volumes of water from the ocean into the ice shell.

Appendix A: Relaxation Timescales of the Ice Shell

The surface deformation produced during and after sill injection depends on the mechanical deformation of the ice shell in response to stresses. Ice deformation will be brittle, elastic, or ductile depending on temperature and depth in the ice shell. The uppermost part of the ice shell is cold, brittle, and likely fractured. Its strength is governed by friction. The warm ice at the base of the ice shell is ductile and accommodates stresses by creep. In between the ductile ice and brittle surface layer, ice is elastic and supports internal and surface loads by flexure. The thickness of the elastic layer depends on time: the viscoelastic relaxation time is

$$\tau_{\text{relax}} = \eta/E, \tag{A1}$$

where E is Young's modulus and the ice viscosity η is

$$\eta(T) = \eta_0 \exp \left[\frac{Q^*}{RT} \left(\frac{T_m}{T} - 1 \right) \right], \tag{A2}$$

with Q^* the activation energy, T_m the melting temperature, and η_0 the viscosity at T_m [Goldsby and Kohlstedt, 2001]; see Table 1 for the parameters.

Figure A1 shows the temperature distribution and τ_{relax} for an ice shell with thickness Z_c in which heat transport occurs by thermal conduction. If convection occurs in the shell, our results apply to the conductive part of the shell only, with Z_c representing the thickness of the conductive part of the shell. The nonlinearity of temperature arises from the temperature dependence of thermal conductivity $k_i(T)$ (Table 1). The relevant thickness of the elastic layer will vary over relevant timescales: on injection timescales it will be thicker

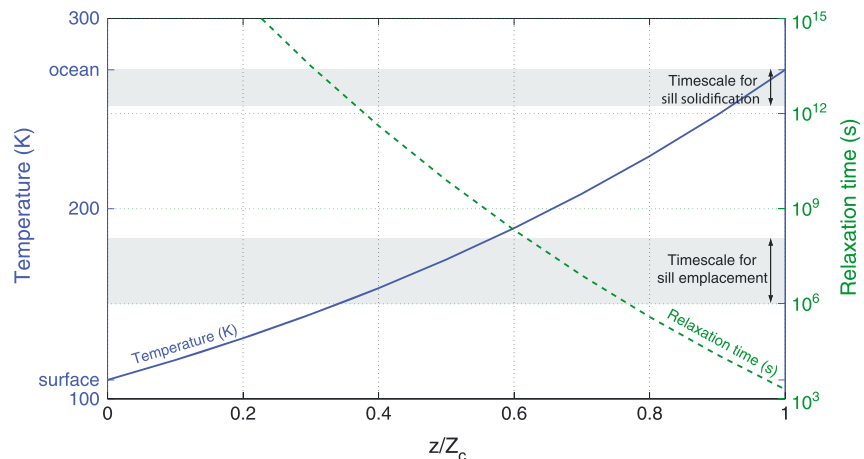


Figure A1. Steady state conductive temperature distribution and relaxation time (η/E) as a function of depth z normalized by the ice shell thickness Z_c for the parameters listed in Table 1.

than that for subsequent evolution of the sill including flexural support after emplacement and final solidification. We have neglected the effects of heating from tidal dissipation on the temperature distribution. However, tidal heating occurs in the warmest ice at the base of the ice shell [Nimmo *et al.*, 2007] where the relaxation time is already short and comparable to the tidal periods.

Appendix B: Scaling Laws for a Deep Axisymmetric Sill

Since lenticulae are circular to elliptical, considering an axisymmetric geometry for the spreading of water sills might be more appropriate. However, an axisymmetric geometry implies water injection through a circular conduit of diameter $2w$, a geometry less probable than an elongated fracture such as a dyke. Terrestrial laccoliths are indeed usually elliptical and generally result from feeding through elongated dykes [Rocchi *et al.*, 2002].

Using a range of upward flow velocities of ~ 1 to 10 m s^{-1} and conduit radius of 1 to 10 m, the injection rate Q_0^r takes values between ~ 3 and $3000 \text{ m}^3 \text{ s}^{-1}$. These values are in good agreement with 3-D injection rates deduced from 2-D values obtained in section 3.1.

Here we develop the analytical solution for the spreading of an axisymmetric deep sill of water, neglecting friction loss, and discuss the implications for the morphology of a shallow axisymmetric sill.

In the case of a deep sill of water, emplaced below a rigid boundary, the driving pressure for the sill is the elastic pressure required for bending the lower elastic layer of ice:

$$P(t)^{\text{deep}} = D_l \nabla_r^4 h(r, t), \quad (\text{B1})$$

where $\nabla_r^4 = \frac{1}{r} \frac{\partial}{\partial r} \left(r \frac{\partial}{\partial r} \left(\frac{1}{r} \frac{\partial}{\partial r} \left(r \frac{\partial}{\partial r} \right) \right) \right)$. As for the 2-D case, for simplicity, the pressure is assumed constant over the sill radius, which gives the shape h of the sill as a function of the sill radius R , using the boundary conditions $h(R) = \left(\frac{\partial h}{\partial r} \right)_R = 0$

$$h(r, t) = \frac{P(t)^{\text{deep}}}{64D_l} R(t)^4 \left(1 - \frac{r^2}{R(t)^2} \right)^2. \quad (\text{B2})$$

Conservation of mass for a constant injection rate Q_0^r (in $\text{m}^3 \text{ s}^{-1}$) (B3) gives the expression that relates the pressure in the sill to the sill radius and time t (B4)

$$Q_0^r t = 2\pi \int_0^{R(t)} h(r, t) r dr, \quad (\text{B3})$$

$$Q_0^r t = \frac{P(t)^{\text{deep}} \pi R(t)^6}{192D_l}. \quad (\text{B4})$$

As for the 2-D case, at the tip, the pressure necessary for bending the lower elastic layer is balanced by inertia

$$\frac{1}{2} \rho_w \left(\frac{dR}{dt} \right)^2 = P(t)^{\text{deep}}, \quad (\text{B5})$$

which, by integration, gives the evolution of the radius R and maximum sill thickness-with-time, using (B4), as well as the thickness-to-radius relationship during the spreading phase

$$R(t) = 2\sqrt{2} \left(\frac{2Q_0^r D_l}{3\pi \rho_w} \right)^{1/8} t^{3/8}, \quad (\text{B6})$$

$$h_0(t) = \left(\frac{3^5 (Q_0^r)^3 \rho_w}{2^{13} \pi^3 D_l} \right)^{1/4} t^{1/4}, \quad (\text{B7})$$

$$h_0(R) = \left(\frac{3^4 (Q_0^r)^2 \rho_w}{2^{13} \pi^2 D_l} \right)^{1/3} R^{2/3}. \quad (\text{B8})$$

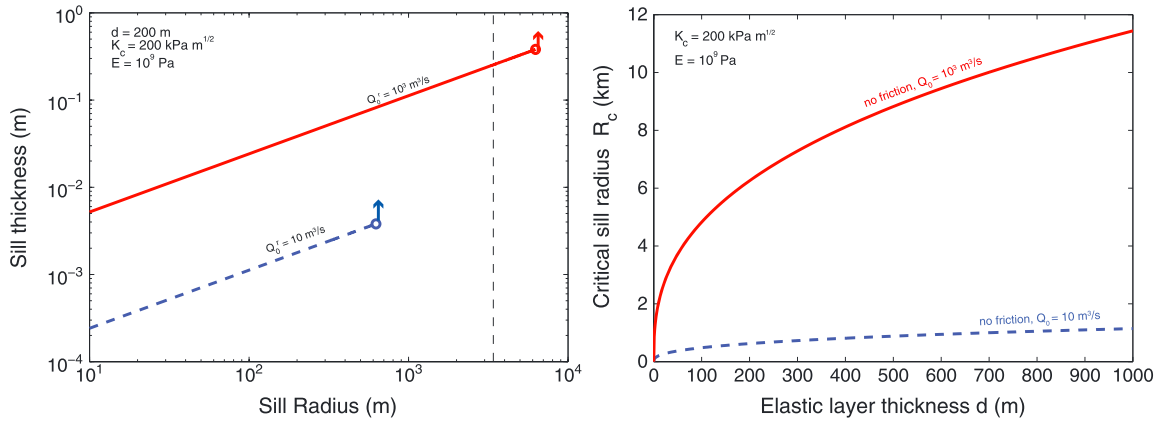


Figure B1. (left) Morphology of an axisymmetric sill during the spreading phase, with model parameters indicated on the graph. (right) Critical radius at which the sill stops spreading as a function of the underlying layer elastic thickness for different values of the injection rate. Friction is neglected in these calculations.

Sill spreading stops once the stress intensity factor for a mode I fracture $K_I = K_M M_0 d_I^{-3/2}$ reaches the fracture toughness limit K_c , where $K_M = 1.932$ and M_0 is the moment about the crack tip and is given by [Bunger and Detournay, 2005; Dyskin et al., 2000]

$$M_0 = \frac{E d_I^3}{12(1-\nu^2)} \left(\frac{\partial^2 h}{\partial r^2} \right)_{r=R(t)} = \frac{E d_I^3}{12(1-\nu^2)} \frac{8h_0(t)}{R(t)^2}. \quad (\text{B9})$$

The critical radius of the sill R_c at which the fracture toughness limit is reached is thus

$$R_c = \left(\frac{K_M}{K_c} \right)^{3/4} \left(\frac{\rho_w}{6} \right)^{1/4} \left(\frac{Q_0^2 E}{\pi(1-\nu^2)} \right)^{1/2} d_I^{3/8}. \quad (\text{B10})$$

For emplacement above an elastic layer of a few hundred meters thick, the critical radius of an axisymmetric sill at which the ice fracture toughness is reached and spreading stops is between ~ 1 and 10 km, when friction is assumed negligible (Figure B1), similar to the case of a 2-D sill. The thickness of the sill is then about 1 order of magnitude smaller than for a 2-D sill. As for a 2-D shallow sill, the spreading of an axisymmetric shallow sill will be promoted because of sill weight when the sill radius reaches $4\Lambda_u$, with Λ_u the flexural parameter of the overlying elastic layer. For an elastic layer a few hundred meters thick, the radius at which gravity becomes dominant for sill spreading is a few kilometers (Figure B1) and the sill thickness is then less than a meter. Our conclusions regarding spreading of shallow versus deep sills thus still hold for an axisymmetric geometry.

Appendix C: Pressure Gradient Within the Sill

Here we examine the effects of a pressure gradient within the bulk of the flow. When friction is dominant and the friction factor evolves with $Re^{-1/4}$ (17), we can obtain from (16) that the mean horizontal velocity within the flow \bar{u} varies with the horizontal pressure gradient $\nabla P = \frac{\partial P}{\partial x}$ as

$$\bar{u} = -5 \left(\frac{h^5}{\mu_w \rho_w^3 |\nabla p|^3} \right)^{1/7} \frac{\partial P}{\partial x}, \quad (\text{C1})$$

which is equivalent to equation (8.c) from Lister and Kerr [1991] by a factor 1.6. In order to evaluate the effect of a pressure gradient on the evolution of the flow morphology, we assume that the velocity varies linearly with the pressure gradient and hence that $|\nabla p|$ is constant, as for dyke propagation in Lister and Kerr [1991]. In our problem, we approximate the value of $|\nabla p|$ by

$$|\nabla p| \approx \frac{D_I}{\Lambda_I^4} = \rho_w g. \quad (\text{C2})$$

In that case, the effects of a pressure gradient within the flow are overestimated, since \bar{u} evolves with $\left(\frac{\partial P}{\partial x} \right)^{4/7}$ while in the “uniform pressure” solution, these effects are underestimated.

Using the expression for the pressure in a deep sill (8) to calculate the pressure gradient and the conservation of mass $\frac{\partial h}{\partial t} = -\frac{\partial}{\partial x}(\bar{u}h)$, we obtain the following equation

$$\frac{\partial h}{\partial t} = \frac{5D_l}{(\mu_w \rho_w^3 |\nabla p|^3)^{1/7}} \frac{\partial}{\partial x} \left(h^{12/7} \frac{\partial^5 h}{\partial x^5} \right). \quad (C3)$$

This equation is of the form $\frac{\partial h}{\partial t} = B \frac{\partial}{\partial x} \left(h^n \frac{\partial^5 h}{\partial x^5} \right)$, with $B = \frac{5D_l}{(\mu_w \rho_w^3 |\nabla p|^3)^{1/7}}$ and $n = 12/7$. The flow of a Newtonian fluid below a thin elastic plate, when gravity is negligible, also respects this equation with $B = \frac{D}{12\mu}$ and $n = 3$ [Michaut, 2011; Lister et al., 2013]. These types of equations have been mathematically analyzed in detail by Flitton and King [2004]. We follow the proof of Flitton and King [2004] and suppose that (C3) has a solution with a propagating contact line with an asymptotic traveling-wave behavior $h(x, t) \sim A(t)(L(t) - x)^\alpha$ as $x \rightarrow L(t)$, where A and α are strictly positive and $h = 0$ for $x \geq L(t)$. At the front, the time derivative is dominated by its convective part and the dominant balance is

$$\frac{dL}{dt} A(t) \alpha (L(t) - x)^{\alpha-1} = B A(t)^{19/7} \alpha (\alpha - 1)(\alpha - 2)(\alpha - 3)(\alpha - 4) \left(\frac{19}{7} \alpha - 5 \right) (L(t) - x)^{19\alpha/7-6}. \quad (C4)$$

By equating the exponent of $L(t) - x$, we have $\alpha = 35/12$ and obtain

$$\frac{dL}{dt} = 0.46 B A(t)^{12/7}, \quad (C5)$$

which is positive. Hence, (C3) has a spreading contact line solution (i.e., $dL/dt > 0$), as shown by Flitton and King [2004], for $5/3 < n = 12/7 < 5/2$. In that case, there is no need to invoke a specific physical process for spreading to occur at the front such as a prewetting film or a fluid lag, as in the case of a Newtonian fluid. Spreading occurs because of the pressure gradient within the bulk of the flow, and the large-time behavior is given by the mass-preserving similarity solution as shown by Flitton and King [2004] for a constant volume flux.

In the case of a constant volume flux, as considered here, the mass-preserving similarity solution is found by introducing the variable $\eta = x/t^\alpha$ and decomposing h into

$$h(x, t) = f(\eta) t^\beta, \quad (C6)$$

where η and β are to be determined. Conservation of mass (15) requires that $\beta = 1 - \alpha$, and using (C6) in (C3), we obtain

$$t^{-\alpha} \left((1 - \alpha) f - \alpha \eta \frac{df}{d\eta} \right) = B t^{19/7-61/7\alpha} \frac{d}{d\eta} \left(f^{12/7} \frac{d^5 f}{d\eta^5} \right), \quad (C7)$$

which gives, by equating the exponent of t , $\alpha = 19/54$, and hence the length and thickness of the flow evolve as

$$h(\eta, t) = f(\eta) t^{35/54} \quad (C8)$$

$$L(t) = \eta_L t^{19/54} \quad (C9)$$

$$h_0 \propto L^{35/19}. \quad (C10)$$

The shape function $f(\eta)$ and constant η_L have to be solved numerically.

We numerically solved (C3) using the method described in Michaut [2011]. To stabilize the numerical results, we use a prewetting film of negligible thickness of 10^{-4} to $10^{-3}H$, where H is the characteristic thickness of the flow given by $H = \left(\frac{\mu_w \Lambda_l^7 Q_0^7}{\rho_w g^4} \right)^{1/19}$. The characteristic flow length is given by the flexural wavelength Λ_l and the characteristic time by $H \Lambda_l / Q_0$. The prewetting film thickness does not have an influence on the results as predicted by Flitton and King [2004].

We verify that the spreading, over the time interval that we can obtain numerical solutions, tends to the similarity solution given by (C10) for a constant injection rate (Figures C1a and C1b). Although this solution accounts for, and overestimates the effects of, pressure gradients in the flow, it remains close to the simple “uniform pressure” solution. The shape of the flow is also close to the “uniform pressure” solution (14) (Figure C1c). This is because the pressure gradient is largest at the ends of the sill as is typical of flows below

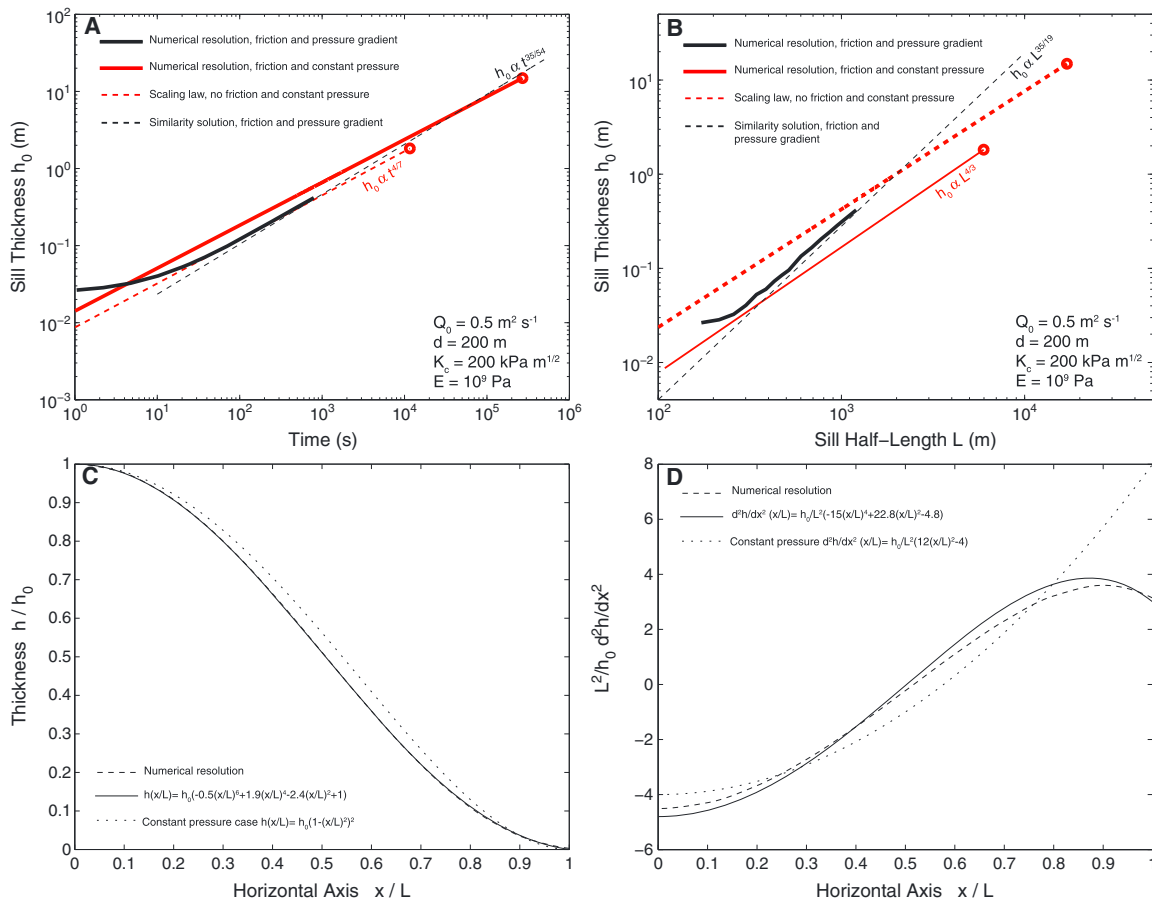


Figure C1. Sill maximum thickness as a function of (a) time and (b) sill half-length, comparison between the numerical solution accounting for pressure gradient effects in the bulk of the flow (thick black line), which follows, at large time, the similarity solution (black dashed line) described by (C10) and the simple numerical solution assuming a uniform pressure within the flow described in the main text with or without friction (red solid line and red dashed line, respectively). Parameters are indicated on the graphs. All the different solutions give consistent and similar results. (c) The shape of the flow calculated numerically and accounting for friction and a pressure gradient is well fitted by (C11) and is close to the solution for a constant pressure given by (14). (d) The second derivative of the flow thickness with horizontal coordinate calculated using the full numerical solution accounting for friction and pressure gradient is well fitted by the second derivative of (C11). At the tip, it is of the same order of magnitude as the second derivative of (14).

an elastic layer [Flitton and King, 2004; Lister et al., 2013]. The uniform pressure solution provides a good approximation that allows the evolution of flow morphology and pressure to be derived over the timescale of intruding the sill.

Furthermore, the shape of the flow is very well fitted by the sixth-order polynomial

$$h_p(x) = h_0 \left(-0.5 \frac{x^6}{L^6} + 1.9 \frac{x^4}{L^4} - 2.4 \frac{x^2}{L^2} + 1 \right), \quad (C11)$$

whose second and fourth derivatives as a function of x also fit very well the second and fourth derivatives of the flow thickness calculated numerically (see Figures C1c and C1d). The dimensionless value of the second derivatives of the flow thickness $\frac{L^2}{h_0} \frac{\partial^2 h}{\partial x^2}$ obtained from these simulations is also similar to the one obtained using the “uniform pressure” solution, though smaller by a factor of ~ 2 at the tip (Figure C1d). However, the ratio $\frac{h_0}{L^2}$ also becomes larger by an equivalent factor for the case accounting for pressure gradient in the bulk of the flow, since the thickness grows more rapidly with sill length (see Figure C1b), and the moments at the tip are thus similar for a given thickness and sill length of approximately a few kilometers.

Appendix D: Thermal Anomaly in a Spreading Sill

We consider the cooling of a deep sill. As the sill spreads, it advects heat while heat is being conducted to the surrounding ice. Here we investigate the position within the sill as a function of time where the

heat advected with the liquid water and the heat loss by conduction are of similar magnitude in order to deduce the evolution of the size of the thermal anomaly (where heat advection dominates over cooling) and associated cooling front (where cooling dominates over advection).

The equation for heat transport within the sill is given by

$$\rho_w C_w \frac{d(hT)}{dt} = -k_w \frac{dT}{dz} \Big|_{z=0} + k_w \frac{dT}{dz} \Big|_{z=h}, \quad (D1)$$

where the terms on the right are heat loss by conduction at the top and bottom of the sill. To estimate these terms, we assume a parabolic vertical temperature profile, as the parabolic contribution is dominant over higher-order terms when estimating heat loss by conduction [Bercovici and Lin, 1996]. Neglecting heating of the wall during sill intrusion, we use a constant temperature condition at the bottom and top of the sill, equal to T_0 , i.e., $T_{z=0} = T_{z=h} = T_0$ and a (maximum) temperature equal to the injection temperature T_m at the flow center, and calculate

$$T(z) - T_0 = \frac{4\Delta T}{h^2}(hz - z^2), \quad (D2)$$

where $\Delta T = T_m - T_0$.

Introducing (D2) into (D1), we obtain

$$\frac{d(hT)}{dt} = -\frac{8\kappa\Delta T}{h}. \quad (D3)$$

We identify the position x_f in the intrusion where heat loss by conduction balances the heat advected with water. For $x < x_f$ we assume $\frac{d(hT)}{dt} \approx \Delta T \frac{dh}{dt}$, and we have

$$\Delta T \frac{dh}{dt} \equiv \frac{8\kappa\Delta T}{h}. \quad (D4)$$

From the shape of the sill given by (14), we deduce

$$\frac{dh}{dt} = \left(1 - \frac{x^2}{L(t)^2}\right) \left[\frac{dh_0}{dt} \left(1 - \frac{x^2}{L(t)^2}\right) + 4h_0(t) \frac{x^2}{L^3} \frac{dL}{dt}\right]. \quad (D5)$$

The thermal diffusivity of liquid water is relatively small and hence, for thicknesses h larger than ~ 1 cm, the term on the right side of (D3) is small during sill spreading, and cooling is limited to a small zone of size $\left(1 - \frac{x_f}{L}\right)$ at the tip of the sill. Assuming $\xi = \left(1 - \frac{x_f}{L}\right) \ll 1$, i.e., that $x_f \sim L$, we obtain

$$\Delta T \frac{dh}{dt} \approx \Delta T \xi \frac{4h_0(t)}{L(t)} \frac{dL}{dt} \equiv \frac{8\kappa\Delta T}{h(x_f, t)}. \quad (D6)$$

With $\left(1 - \frac{x_f^2}{L^2}\right) = \left(1 - \frac{x_f}{L}\right) \left(1 + \frac{x_f}{L}\right) \approx 2\xi$, we have $h(x_f, t) \approx 4h_0(t)\xi^2$ from (14) and

$$\xi^3 = \kappa \frac{L(t)}{4h_0(t)^2} \left(\frac{dL}{dt}\right)^{-1}. \quad (D7)$$

Using the expressions for h_0 , L and dL/dt as a function of time given by equations (20), (21), and (23), we obtain the evolution of the front size relative to the sill half-length ξ .

$$\xi(t) = \left(\frac{4}{15}\right)^{2/3} \left(\frac{7}{3}\right)^{11/21} \left(\frac{90D_l}{\rho_w}\right)^{2/21} Q_0^{-4/7} \kappa^{1/3} t^{-1/21}. \quad (D8)$$

The relative front size ξ decreases as the injection rate increases, because heat advection is then more important; it increases with the flexural rigidity of the elastic layer D_l since the flow is then thinner and cools more rapidly. Because the sill inflates over its whole area, the front size ξ also decreases with time. However, the exponent characterizing the temporal evolution of ξ is very small ($-1/21$) and the relative front size is thus quite stable: for $t = 1$ to 10^5 s, $Q_0 = 0.5$ to 1 m² s⁻¹, d_l of a few hundred meters, and ξ is between one twentieth and one tenth of the sill half-length L . Hence, the hot thermal anomaly grows with the sill, extending at least approximately nine tenths of its length.

If freezing occurs at the tip of the sill, and the spreading is not limited by fracture toughness but governed by bending of the elastic layers, heat advection within the sill should allow the sill to continue to spread. If friction is important, freezing could also decrease the aperture for the flow at the front, decreasing its propensity to spread (see, for instance, (C3)); this effect could be counterbalanced by an accompanying increase in the pressure gradient $\frac{\partial^5 h}{\partial x^5}$ since freezing is more important where the thickness is smaller. However, this depends on the exact shape of the front and the potential feedback between freezing and spreading requires a more detailed solution. However, the extent of the cooling front can be estimated at approximately one twentieth to one tenth of the intrusion length. When the pressure in the sill is then such that the stress intensity factor equals the fracture toughness of ice and the sill half-length is larger than 1 km, the cold front is likely to be large enough to allow for total freezing and closing of the crack, impeding further lateral growth of the sill.

Acknowledgments

The authors are grateful to Allan Rubin and Francis Nimmo for providing careful and thoughtful reviews on the manuscript. The authors thank IPGP for hosting M. Manga's visit in Paris. This work was supported by PNP/INSU (C. Michaut) and NASA (M. Manga).

References

- Barr, A. C., and A. P. Showman (2009), Heat transfer in Europa's icy shell, in *Europa after Galileo*, pp. 405–430, Univ. of Arizona Press, Tucson, Ariz.
- Bercovici, D., and J. Lin (1996), A gravity current model of cooling mantle plume heads with temperature-dependent buoyancy and viscosity, *J. Geophys. Res.*, *101*, 3291–3309.
- Billings, S. E., and G. W. Kattenhorn (2005), The great thickness debate: Ice shell thickness models for Europa and comparisons with estimates based on flexure at ridges, *Icarus*, *177*, 397–412.
- Bunger, A. P., and E. Detournay (2005), Asymptotic solution for a penny-shaped near-surface hydraulic fracture, *Eng. Fract. Mechan.*, *72*, 2468–2486.
- Carr, M. H., et al. (1998), Evidence for a subsurface ocean on Europa, *Nature*, *391*, 363–365.
- Collins, G. C., and F. N. Nimmo (2009), Chaotic terrain on Europa, in *Europa after Galileo*, pp. 259–281, Univ. of Arizona Press, Tucson, Ariz.
- Collins, G. C., J. W. Head, R. T. Pappalardo, and N. A. Spaun (2000), Evaluation of models for the formation of chaotic terrain on Europa, *J. Geophys. Res.*, *105*, 1709–1716.
- Craft, K. L., W. Patterson, and R. T. Lowell (2013), Sill emplacement in Europa's ice shell as a mechanism for double ridge formation, paper presented at 44th Lunar and Planetary Science Conference, Woodlands, Tex.
- Crawford, G. D., and D. J. Stevenson (1988), Gas-driven water volcanism in the resurfacing of Europa, *Icarus*, *73*, 66–79.
- Dombard, A. J., G. W. Patterson, A. P. Lederer, and L. M. Prockter (2012), Flanking fractures and the formation of double ridges on Europa, *Icarus*, *223*, 74–81.
- Dyskin, A. V., L. N. Germanovich, and K. B. Ustinov (2000), Asymptotic analysis of crack interaction with free boundary, *Int. J. Sol. Struct.*, *37*, 857–886.
- Fagents, S. A. (2003), Considerations for effusive cryovolcanism on Europa: The post-Galileo perspective, *J. Geophys. Res.*, *108*, 5139, doi:10.1029/2003JE002128.
- Fine, R. A., and F. J. Millero (1973), Compressibility of water as a function of temperature and pressure, *J. Chem. Phys.*, *59*, 5529–5536.
- Flitton, J. C., and J. R. King (2004), Moving-boundary and fixed-domain problems for a sixth-order thin-film equation, *Eur. J. Appl. Math.*, *15*, 713–754.
- Goldsby, D. L., and D. L. Kohlstedt (2001), Superplastic deformation of ice: Experimental observations, *J. Geophys. Res.*, *106*, 11,017–11,030.
- Goodman, J. C., G. C. Collins, J. Marshall, and R. T. Pierrehumbert (2004), Hydrothermal plume dynamics on Europa: Implications for chaos formation, *J. Geophys. Res.*, *109*, E03008, doi:10.1029/2003JE002073.
- Greenberg, R., G. V. Hoppa, B. R. Tufts, P. Geissler, J. Riley, and S. Kadel (1999), Chaos on Europa, *Icarus*, *141*, 263–286.
- Greenberg, R., P. Geissler, G. Hoppa, and B. R. Tufts (2002), Tidal-tectonic processes and their implications for the character of Europa's icy crust, *Rev. Geophys.*, *40*(2), 1004, doi:10.1029/2000RG000096.
- Griffiths, R. W., and I. H. Campbell (1991), Interaction of mantle plume heads with the Earth's surface and onset of small-scale convection, *J. Geophys. Res.*, *96*, 18,295–18,310.
- Gudmundsson, A. (2011), *Rock Fractures in Geological Processes*, Cambridge Univ. Press, Cambridge, U. K.
- Han, L., and A. P. Showman (2005), Thermo-compositional convection in Europa's icy shell with salinity, *Geophys. Res. Lett.*, *32*, L20201, doi:10.1029/2005GL023979.
- Han, L., and A. P. Showman (2010), Coupled convection and tidal dissipation in Europa's ice shell, *Icarus*, *207*, 834–844.
- Head, J. W., and T. T. Pappalardo (1999), Brine mobilization during lithospheric heating on Europa: Implications for formation of chaos terrain, lenticula texture, and color variations, *J. Geophys. Res.*, *104*, 27,143–27,155.
- Hussmann, H., T. Spohn, and K. Wieczerkowski (2002), Thermal equilibrium states of Europa's ice shell: Implications for internal ocean thickness and heat flow, *Icarus*, *156*, 143–151.
- Klinger, J. (1980), Influence of a phase transition of ice on the heat and mass balance of comets, *Science*, *209*, 271–272.
- Koch, D. M., and D. L. Koch (1995), Numerical and theoretical solutions for a drop spreading below a free fluid surface, *J. Fluid Mech.*, *287*, 251–278.
- Lister, J. R., and R. C. Kerr (1991), Fluid-mechanical models of crack propagation and their application to magma transport in dykes, *J. Geophys. Res.*, *96*, 10,049–10,077.
- Lister, J. R., G. G. Peng, and J. A. Neufeld (2013), Viscous control of peeling an elastic sheet by bending and pulling, *Phys. Rev. Lett.*, *111*, 1–5, doi:10.1103/PhysRevLett.111.154501.
- Litwin, K. L., B. R. Zyguelbaum, P. J. Polito, L. S. Sklar, and G. C. Collins (2012), Influence of temperature, composition, and grain size on the tensile failure of water ice: Implications for erosion on titan, *J. Geophys. Res.*, *117*, E08013, doi:10.1029/2012je004101.
- Liu, H. W., and K. J. Miller (1979), Fracture toughness of fresh-water ice, *J. Glaciol.*, *86*, 135–143.
- Manga, M., and C.-Y. Wang (2007), Pressurized oceans and the eruption of liquid water on Europa and Enceladus, *Geophys. Res. Lett.*, *34*, L07202, doi:10.1029/2007GL029297.
- Marsh, B. D. (1989), Magma chambers, *Ann. Rev. Earth Planet. Sci.*, *17*, 39–74.
- McKinnon, W. B. (1999), Convective instability in Europa's floating ice shell, *Geophys. Res. Lett.*, *26*, 951–954.

- Michaut, C. (2011), Dynamics of magmatic intrusions in the upper crust: Theory and applications to laccoliths on Earth and the Moon, *J. Geophys. Res.*, *116*, B05205, doi:10.1029/2010JB008108.
- Michaut, C., D. Baratoux, and C. Thorey (2013), Magmatic intrusions and deglaciation at mid-latitude in the northern plains of Mars, *Icarus*, *225*, 602–613, doi:10.1016/j.icarus.2013.04.015.
- Moore, W. B., and G. Schubert (2000), The tidal response of Europa, *Icarus*, *147*, 317–319.
- Mottaghy, D., and V. Rath (2006), Latent heat effects in subsurface heat transport modeling and their impact on paleotemperature reconstructions, *Geophys. J. Int.*, *164*, 236–245.
- Nimmo, F. (2004), Non-newtonian topographic relaxation on Europa, *Icarus*, *168*, 205–208.
- Nimmo, F., and B. Giese (2005), Thermal and topographic tests of Europa chaos formation models from Galileo e15 observations, *Icarus*, *177*, 327–340.
- Nimmo, F., and M. Manga (2002), Causes, characteristics and consequences of convective diapirism on Europa, *Geophys. Res. Lett.*, *29*(23), 2109, doi:10.1029/2002GL015754.
- Nimmo, F., and M. Manga (2009), Geodynamics of Europa's ice shell, in *Europa after Galileo*, edited by R. T. Pappalardo, W. B. McKinnon, and K. Khurana, pp. 382–404, Univ. of Arizona Press, Tucson, Ariz.
- Nimmo, F., R. T. Pappalardo, and B. Giese (2003), On the origins of band topography, Europa, *Icarus*, *166*, 21–32.
- Nimmo, F., P. C. Thomas, R. T. Pappalardo, and W. B. Moore (2007), The global shape of Europa: Constraints on lateral shell thickness variations, *Icarus*, *191*, 289–291.
- O'Brien, D. P., P. Geissler, and R. Greenberg (2002), A melt-through model for chaos formation on Europa, *Icarus*, *156*, 152–161.
- Pappalardo, R. T., and A. C. Barr (2004), The origin of domes on Europa: The role of thermally induced compositional diapirism, *Geophys. Res. Lett.*, *31*, L01701, doi:10.1029/2003GL019202.
- Pappalardo, R. T., et al. (1998), Geological evidence for solid-state convection in Europa's ice shell, *Nature*, *391*, 365–368.
- Rathbun, J. A., G. Musser, and S. W. Squyres (1998), Ice diapirs on Europa: Implications for liquid water, *Geophys. Res. Lett.*, *25*, 4157–4160.
- Rocchi, S., D. S. Westerman, A. Dini, F. Innocenti, and S. Tonarini (2002), Two-stage growth of laccoliths at Elba Island, Italy, *Geology*, *30*, 983–986.
- Rubin, A. M. (1993), On the thermal viability of dikes leaving magma chambers, *Geophys. Res. Lett.*, *20*, 257–260.
- Rubin, A. M. (1995), Propagation of magma-filled cracks, *Ann. Rev. Earth Planet. Sci.*, *23*, 287–336.
- Rudolph, M. L., and M. Manga (2009), Fracture penetration in planetary ice shells, *Icarus*, *199*, 536–541.
- Ruiz, J. (2010), Equilibrium convection on a tidally heated and stressed icy shell of Europa for a composite water ice rheology, *Earth Moon Planets*, *107*, 157–167.
- Schmidt, B. E., D. D. Blankenship, G. W. Patterson, and P. M. Schenk (2004), Topographic variations in chaos on Europa: Implications for diapiric formation, *Geophys. Res. Lett.*, *31*, L16703, doi:10.1029/2004GL019978.
- Schmidt, B. E., D. D. Blankenship, G. W. Patterson, and P. M. Schenk (2011), Active formation of 'chaos terrain' over shallow subsurface water on Europa, *Nature*, *479*, 501–505.
- Schulson, E. M. (2001), Brittle failure of ice, *Eng. Fracture Mech.*, *68*, 1839–1887.
- Schulson, E. M. (2006), The fracture of water ice 1h: A short overview, *Meteoritics Planet. Sci.*, *41*, 1497–1508.
- Showman, A. P., and L. Han (2004), Numerical simulations of convection in Europa's ice shell: Implications for surface features, *J. Geophys. Res.*, *109*, E01010, doi:10.1029/2003JE002103.
- Singer, K. N., W. B. McKinnon, and P. M. Schenk (2010), Pits, spots, uplifts, and small chaos regions on Europa: Evidence for diapiric upwelling from morphology and morphometry, paper presented at 41st Lunar and Planetary Science Conference, Woodlands, Texas.
- Sotin, C., J. W. Head, and G. Tobie (2002), Europa: Tidal heating of upwelling thermal plumes and the origin of lenticulae and chaos melting, *Geophys. Res. Lett.*, *29*(8), 1233, doi:10.1029/2001GL013844.
- Spaun, N. A., J. W. Head, G. C. Collins, L. M. Prockter, and R. T. Pappalardo (1998), Conamara chaos region, Europa: Reconstruction of mobile polygonal ice blocks, *Geophys. Res. Lett.*, *25*, 4277–4280.
- Thomson, R., and J. R. Delaney (2001), Evidence for a weakly stratified European ocean sustained by seafloor heat flux, *J. Geophys. Res.*, *106*, 12,335–12,365.
- Thorey, C., and C. Michaut (2014), A model for the dynamics of crater-centered intrusions: Applications to lunar floor-fractured craters, *J. Geophys. Res. Planets*, *119*, 286–312, doi:10.1002/2013JE004467.
- Turcotte, D. L., and G. Schubert (1982), *Geodynamics: Applications of Continuum Physics to Geological Problems*, Wiley, Univ. of Michigan.
- Whitehead, J. A., and D. S. Luther (1975), Dynamics of laboratory diapir and plume models, *J. Geophys. Res.*, *80*, 705–717.
- Worster, M. G., H. E. Huppert, and R. S. J. Sparks (1990), Convection and crystallization in magma cooled from above, *Earth Planet. Sci. Lett.*, *101*, 78–89.